Received 11 December 2023; revised 30 January 2024; accepted 21 February 2024. Date of publication 5 March 2024; date of current version 15 April 2024.

Digital Object Identifier 10.1109/OJCOMS.2024.3373368

Cellular Wireless Networks in the Upper Mid-Band

SEONGJOON KANG[1] (Graduate Student Member, IEEE), MARCO MEZZAVILLA[1] (Senior Member, IEEE), SUNDEEP RANGAN[1] (Fellow, IEEE), ARJUNA MADANAYAKE[2] (Member, IEEE), SATHEESH BOJJA VENKATAKRISHNAN[2] (Senior Member, IEEE), GRÉGORY HELLBOURG[3], MONISHA GHOSH[4] (Fellow, IEEE), HAMED RAHMANI[1] (Member, IEEE), AND ADITYA DHANANJAY[1]

[1]Electrical and Computer Engineering Department, New York University Tandon School of Engineering, Brooklyn, NY 11201, USA

[2]Department of Electrical and Computer Engineering, Florida International University, Miami, FL 33174, USA

[3]Department of Astronomy, California Institute of Technology, Pasadena, CA 91125, USA

[4]Department of Electrical Engineering, University of Notre Dame, Notre Dame, IN 46556, USA

CORRESPONDING AUTHOR: S. KANG (e-mail: sk8053@nyu.edu)

This work was supported in part by NTIA under Grant 36-60-IF003; in part by the National Science Foundation under Grant 1952180, Grant 2133662, Grant 2236097, Grant 2148293, Grant 1925079, Grant 2052764, Grant 2229471, Grant 2329012, Grant 2216332, Grant 1854798, Grant 1902283, Grant 1711625, Grant 1509754, Grant 1904382, Grant 2243346, Grant 2226392, Grant 2128628, Grant 2132700, Grant 2229387, Grant 2229428, Grant 2229497, and Grant 2128497; and in part by the Industrial Affiliates of NYU Wireless.

ABSTRACT The upper mid-band – approximately from 7 to 24 GHz — has recently attracted considerable interest for new cellular services. This frequency range has vastly more spectrum than the highly congested bands below 7 GHz while offering more favorable propagation and coverage than the millimeter wave (mmWave) frequencies. In this regard, the upper mid-band has the potential to provide a powerful and complementary frequency range that balances coverage and capacity. Realizing cellular networks that exploit the full range of these bands, however, presents significant technical challenges. Most importantly, spectrum will likely need to be shared with incumbents including communication satellites, military RADAR, and radio astronomy. Also, the upper mid-band is simply a vast frequency range. Due to this wide bandwidth, combined with the directional nature of transmission and intermittent occupancy of incumbents, cellular systems will likely need to be agile to sense and intelligently use large spatial and frequency degrees of freedom. This paper attempts to provide an initial assessment of the feasibility and potential gains of such adaptive wideband cellular systems operating across the upper mid-band. The study includes: (1) a detailed ray tracing simulation to assess potential gains of multi-band systems in a representative dense urban environment and illustrate the value of a wideband system with dynamic frequency selectivity; (2) an evaluation of potential cross-interference between satellites and terrestrial cellular services and interference nulling to reduce that interference; and (3) design and evaluation of a compact multi-band antenna array structure. Leveraging these preliminary results, we identify potential future research directions to realize next-generation systems in these frequencies.

INDEX TERMS Upper mid-band, 6G, cellular wireless systems, FR3, satellite communications.

I. INTRODUCTION

CELLULAR wireless systems up to the fourth generation (4G) had largely operated in a range of microwave frequencies below 6 GHz. Given the severe spectral shortage in these bands, 5G systems [1], [2] introduced new capabilities in the millimeter wave (mmWave) frequencies above 24 GHz [3], [4], [5]. The wide bandwidths available in the mmWave range, combined with spatial multiplexing capabilities, have enabled massive multi-Gbps peak rates. However, extensive measurements also now show that

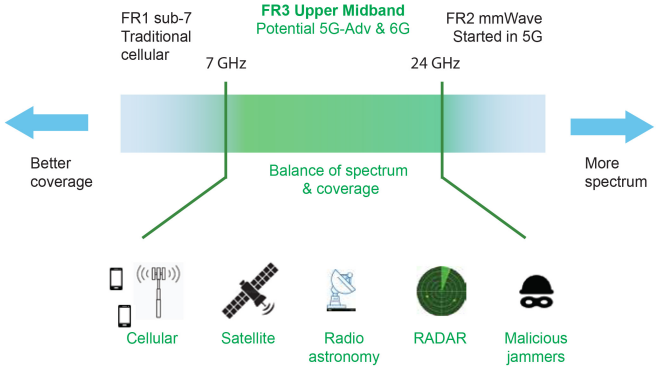

FIGURE 1. The upper mid-band (called frequency range 3 or FR3 in 3GPP) is a potential new band for the cellular services that offers a balance of coverage and spectrum. To utilize the full band, cellular services will likely require sharing spectrum between satellite, and radio astronomy along with resliency to malicious jammers.

practical performance is often intermittent [6], [7] with limited penetration inside [8], [9]. At root, this poor coverage is due to the inherently limited range of mmWave signals and their high susceptibility to blockage [10], [11], [12], [13], [14].

Against this backdrop, the upper mid-band spectrum, roughly from 7-24 GHz, is being considered to provide a good balance of coverage and bandwidth, overcoming the spectral shortage of the sub-6 bands while having favorable propagation and penetration relative to the mmWave frequencies. For these reasons, the band has recently attracted considerable attention for commercial cellular communications and has been cited by industry as a leading candidate spectrum for next generation (NextG, 5G and beyond) wireless networks [15], [16], [17], [18]. The Federal Communications Commission (FCC) Technical Advisory Committee (TAC) has recently identified the upper mid-band as vital for meeting the growing data rate demands [19], [20]. The 3rd Generation Partnership Project (3GPP), the organization that sets cellular standards, has also begun study of these bands [21] – see Section II for more details.

In 3GPP, the upper mid-band is referred to as Frequency Range 3 (**FR3**). FR1 initially referred to the traditional spectrum below 6 GHz, which was later expanded to 7.125 GHz [22]. FR2 refers to the mmWave spectrum that was introduced in the fifth generation (5G) standard.

A. CHALLENGES

Development of cellular services in the full range of these bands faces significant challenges:

- *Need for sensing and spectrum sharing with incumbents:* Most importantly, these bands are already used by several vital incumbent services. This situation stands in contrast to the mmWave deployments where the bands were significantly less occupied. As we review in Section II-C, commercial satellite services already widely use these bands and have been interested in increased bandwidth allocations, particularly for broadband rural access. The upper mid-band is also vital for military and commercial RADAR and contains scientifically important spectral lines that are fundamental for radio astronomy.
- *Large spectral range:* The upper mid-band is simply a vast range of spectrum – well beyond the span of most commercial cellular front-ends that typically operate over a small percentage of the carrier frequency. This large range, combined with the need to dynamically share spectrum and directionally transmit, demands new front-ends that adaptively and intelligently sense and exploit large bandwidth and spatial degrees of freedom.
- *Spectral resiliency:* Sensing capabilities, combined with the ability to adapt in space and frequency, can also yield improved defenses to external attacks from jammers and signal disruption. Such features can provide robust protection for vital future cellular infrastructure.

B. CONTRIBUTIONS

The broad goal of this paper is to assess the feasibility and potential of agile wideband cellular systems operating in these bands. We will also identify key challenges and areas for research. Towards this end, our contributions are:

- *Channel modeling and estimation of multi-band coverage*: We briefly review channel measurements in the upper mid-band range and discuss open areas of research (Section III-A). Also, based on current propagation models, we conduct a ray-tracing simulation in a representative dense urban area (New York City) to assess the coverage and capacity of a potential cellular system in the upper mid-band (Section III-B). Our results demonstrate that mobiles that can adaptively select one of multiple bands across the upper mid-band can improve coverage and data rates over mobiles restricted to a single band. This finding argues for multi-band, adaptive systems to gain the full benefits of the frequency range.
- *Interference with incumbents:* We perform an additional ray tracing simulation (Section IV-B) to assess the potential interference of terrestrial cellular services on the satellite uplink. The analysis shows that interference from both user equipment (UEs) and base stations (BSs) can be significant, but directional nulling can be effective in mitigating the interference with some loss in the terrestrial network capacity. We also discuss some potential interference issues with passive radio astronomy in the upper mid-band.
- *Wideband antenna systems:* Finally, we present (Section V) a compact, multi-band antenna array to demonstrate the feasibility of front-ends that operate over the entire upper mid-band in a small form factor.

II. BACKGROUND AND STANDARDIZATION LANDSCAPE

A. PRIOR DEVELOPMENTS IN THE SUB-6 AND MMWAVE BANDS

The interest in the upper mid-band has to be seen in the context of developments of commercial cellular systems in both the sub-7 and mmWave frequency ranges over the last decade. Early mmWave experiments and capacity analyses such as [3], [4], [23], [24] suggested the possibility of massive data rates in micro-cellular deployments owing to the wide bandwidths and spatial multiplexing gains available in the mmWave frequencies. Based partially on these and other results, the mmWave bands emerged as an integral component of the 5G New Radio (NR) specification [1], [2]. Commercial mmWave deployments appeared shortly after the release of the specification, particularly in the U.S. [5].

Coverage at reasonable cell densities in these deployments, however, has been an enormous challenge. Several recent measurements in commercial mmWave networks now clearly demonstrate that outdoor coverage can be highly intermittent [6], [7] with limited penetration indoors [8], [9]. MmWave signals are simply blocked by many common building materials such as concrete [10], [14] as well as the human body and other obstacles [11], [12], [13]. See also Section III-D below.

Parallel to the developments in the mmWave, significant spectrum was also released in portions of the mid-band frequencies above 3 GHz, including the Citizens Broadband Radio Service (CBRS) band (3.55 to 3.7 GHz) [25] and the C-band [26] (3.7 to 4.2 GHz). These bands were instrumental for both so-called private 5G networks [27] as well as spectrum expansion in many wide area public networks. More recently, there has also been significant discussion of unlicensed bands from approximately 6 to 7 GHz, extending the mid-band further [22]. In particular, both wireless LAN and cellular services have been considering enhancements to operate in these bands [28], [29].

Measurements from commercial network monitoring companies, now offer an opportunity to compare the practical performance of these networks. On the one hand, Ookla reported in 2022 [30] that the tested mmWave networks offer an incredible 1.6 Gbps median downlink throughput, up to seven times higher than systems in C-band. Similarly, in 2021, Open Signal demonstrated [31] that Verizon's mmWave downlink capacity was at least three times as high as networks relying mostly on mid-band spectrum. Nevertheless, networks with mid-band alone often provided downlink speeds in the hundreds of Mbps. Moreover, the coverage for mid-band networks was much more uniform than mmWave. For example, Open Signal's study [31] showed that users connect to mmWave less than 1% of the time.

B. RECENT STANDARDIZATION EFFORTS IN THE UPPER MID-BAND

The relative success of commercial cellular systems in the mid-band, combined with the high data rates, but intermittent coverage, of mmWave has set the stage for interest in the upper mid-band. The hope is to provide the high data rates close to those available in the mmWave range, but with much more uniform coverage. As mentioned in the Introduction, the bands have been identified by industry [15], [16] and 3GPP has recently formally started study of services in the 7 to 24 GHz band [17], [21], where they are called frequency range 3 or FR3. Note that, in 3GPP terminology, frequency range 1, or FR1, has been extended from sub-6 GHz to sub-7 GHz to include the frequencies in the 6 to 7 GHz range in FR1 [32].

In 2022, the FCC also began discussion on two 500 MHz bands from 12.2-12.7 GHz [33], and 12.7-13.2 GHz [34] for possible cellular use. While the first band has now been rejected for cellular services, there is wide recognition of the need for opening the upper mid-band for cellular services. For example, the FCC Technical Advisory Committee (TAC) has recently published a comprehensive survey of spectrum from 7.125 to 24 GHz [19] as well as a 6G working paper [20]. These analyses emphasize the need for considering larger portions of the upper mid-band for terrestrial cellular services in order to meet the growing data demand.

C. INCUMBENCY AND THE NEED FOR SPECTRUM SHARING

The FCC TAC analyses [19], [20] also emphasize that a key issue in allocating the upper mid-band is incumbents, particularly commercial satellite services that also need bandwidth. In fact, the rejection of the 12.2-12.7 GHz band proposed in [33] for cellular services was largely due to the interference onto ground satellite units. We will perform some simple cellular-satellite interference calculations in Section IV-B.

The FCC analysis [19] has thus considered several potential models for spectrum sharing in the upper mid-band. Interestingly, spectrum sharing was critical in CBRS and C-Band allocations [35], [36]. Spectrum sharing mechanisms in these bands included spectrum access systems SAS and more general licensed spectrum access (LSA) schemes are now being considered in the upper mid-band as well. More dynamic methods for spectrum sharing, as is being considered by 3GPP [37], [38] could also be used.

In short, the upper mid-band is a vast and valuable frequency range for numerous services. How to allocate and share the spectrum between various users will be one of the fundamental design and policy challenges going forward.

III. COVERAGE AND CAPACITY GAINS

A. PRIOR CHANNEL MEASUREMENTS AND STUDIES

Aspects of channel propagation in the upper mid-band have been studied for over two decades. For example, [40], [41] studied performed indoor radio measurements up to 11.5 GHz in the early and mid-1990s. Significant research has continued. For example, additional indoor measurements can be found in [42] (from 2.4 to 61 GHz)

TABLE 1. Multi-frequency capacity simulation parameters.

Parameters	Values			
Area (m^2)	1120×510			
Inter-site distance between gNBs (m)	200			
Maximum transmit power of gNBs (dBm)	33 dBm (from 3GPP TR 38.141 [49], Table 6.3.1-1, Local Area BS)			
Number of sectors for gNBs	3			
Down-tilted antenna angle of gNBs	$-12°$			
UE Noise figure (dB)	7			
Field pattern of antenna element	Taken from 3GPP TR 37.840 [50]			
Frequency-dependent parameters				
Frequency [GHz]	6	12	18	24
Bandwidth [MHz]	100	200	300	400
BS URA dimensions	2×2	4×4	5×5	7×7
UE ULA dimensions	1×2	1×2	1×3	1×3

and in corridors from 9 to 11 GHz in [43]. Attenuation measurements for various building materials at 800 MHz to 18 GHz were conducted in [44]. Indoor and outdoor 5G diffraction measurements at 10, 20 and 26 GHz can be found in [45]. The work in [46] performed wideband outdoor channel measurements at 3–18 GHz and a more recent comprehensive set of outdoor and indoor measurements at 3.3, 6.5, 15 and 28 GHz was conducted in [47]. Satellite propagation has also been extensively studied – see, for example, [48] on earth satellite measurements at 12 GHz.

A key and consistent finding of these channel measurement studies is that the factors that influence large-scale propagation, such as transmission losses, reflectivity, and diffraction, vary considerably over the upper mid-band. As expected, the lower frequencies in the upper mid-band provide more favorable coverage in most indoor and outdoor scenarios. At the same time, higher frequencies offer better bandwidth since bandwidth allocations generally scale with the carrier frequency.

B. MULTIFREQUENCY OUTDOOR CAPACITY GAINS

One implication of the variability of propagation across the upper mid-band is that cellular systems would ideally have access to bands across the spectrum with real-time band selection. Wideband mobiles could use the higher frequencies with higher bandwidth when coverage is available, and switch to lower frequencies when the higher frequencies are blocked.

To estimate the potential gain of such a multi-band, frequency adaptive system in the upper mid-band, we consider a dense urban area, i.e., Herald Square in New York City, as shown in Fig. 2(a) and downlink scenario (gNB→UE). In dense urban scenarios, capacity a key requirement. At the same time, providing satisfactory coverage is challenging at high frequencies due to blockage, as have been experienced in the mmWave bands [11], [12], [51]. Within this area, we consider a hypothetical systems operating at up to four potential frequencies: 6, 12, 18, and 24GHz.

The simulation parameters of the potential cellular downlink systems at these frequencies are shown in Table 1. Note that the bandwidth in each frequency scales with the carrier, as is typical in deployments today. As shown in Fig. 2(b), the size of the gNB antenna array also scales so that the aperture is approximately constant. Furthermore, in the simulation area, we manually selected the locations of 18 BSs (gNB) on rooftops, corresponding to an inter-site distance (ISD) of approximately 200 m, typical for urban microcellular evaluations. Terrestrial UEs are randomly placed outside buildings, and ray tracing was performed using Wireless Insite [52], which has recently been proven fairly accurate by conducting real-world measurements in the mmWave bands, as reported in [53], [54].

As mentioned in the Introduction, a critical factor in the performance of mmWave systems is the susceptibility of signals to blockage [10], [11], [12], [13], [14]. To model the effect of blockage, we consider two scenarios:

- *No blockage*; and
- *Blockage* modeled with the 3GPP Blockage Model B [55] with $K = 4$ random human blockers.

Fig. 2(c) shows a coverage map of the unblocked wideband SNR for a single BS deployment as an example. As expected, we see that coverage is greatly reduced as frequency increases.

For both the unblocked and blocked cases, we compute the wideband SNR for each UE and BS and assume the UE is served by the BS with the strongest unblocked SNR. Then, given an SNR, we assume the achieved rate R (goodput) follows a standard realistic model [56]:

$$R = B \min\{\rho_{\max}, \alpha \log_2(1 + \mathsf{SNR})\} \tag{1}$$

where B is the bandwidth, α is a system bandwidth loss factor to account for overhead and receiver imperfections, and $\rho_{\max}$ is a maximum spectral efficiency. Following [56], we adopt 0.57 for α and 4.8 for $\rho_{\max}$.

Fig. 3 shows the resulting SNR distribution for frequencies 6, 12, 18 and 24 GHz at all outdoor UE locations in the study area without blockage. As can be seen in Fig. 3, UEs at lower frequencies experience uniformly better SNRs than higher frequencies due to favorable propagation and reduced noise power from using a smaller bandwidth compared to higher frequencies. Fig. 4(a) shows the corresponding rate distribution. We observe that, even though the SNRs are lower, as expected, the use of higher frequencies (18 and 24 GHz) ensures superior data rate due to the wider bandwidth. Note that from (1), there is a maximum rate of $R = B\rho_{\max}$ which corresponds to 0.48, 0.96, 1.44 and 1.92 Gbps at frequencies 6, 12, 18 and 24 GHz, respectively. Hence, higher peak rates can be achieved at higher frequencies, where more bandwidth is available.

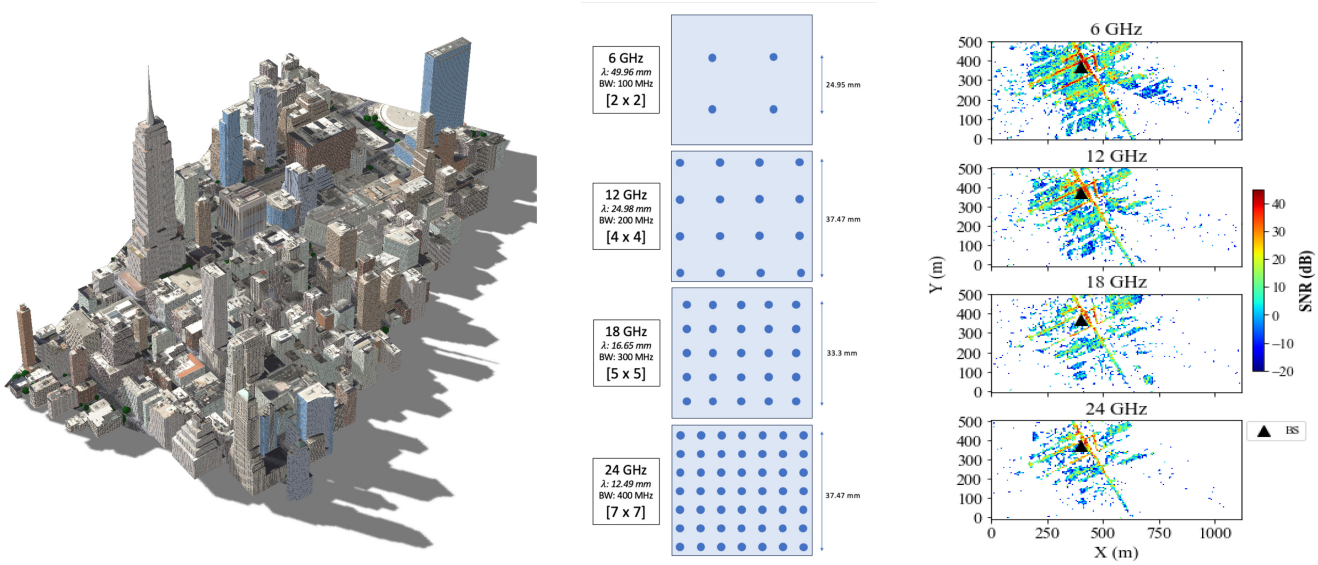

(a) 3D model (b) gNodeB arrays (c) Coverage

FIGURE 2. Simulation results obtained via ray-tracing a dense urban area of NYC at four frequencies in the upper mid-band for one example BS site. Left: 3D model of the NYC area (Herald Square) that was used for raytracing. The model was downloaded from [39], which enabled a fairly accurate mapping of foliage and building materials. Center: gNodeB antenna array architecture and bandwidth at each carrier frequency. Right: Coverage map obtained from raytracing data from an example single BS. The reduced coverage with higher frequencies is readily visible.

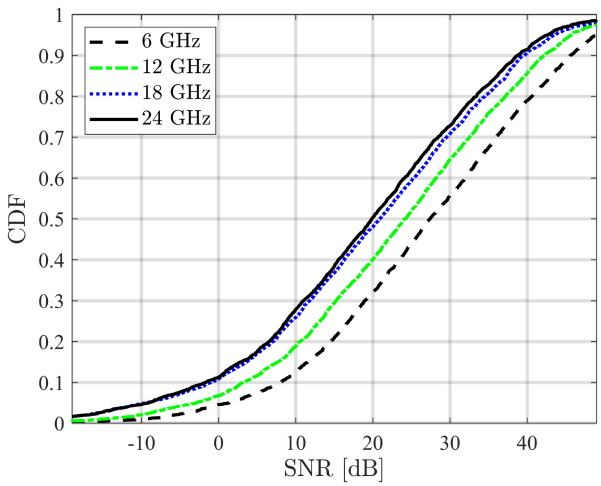

FIGURE 3. Aggregate multi-band SNR distribution for all outdoor UEs without blockage.

However, UEs at the cell edge (for example, UEs up to the bottom 10% percentile of the CDF) suffer a significantly worse rate in the higher frequency bands (18 and 24 GHz) compared to UEs at lower frequencies (6 and 12 GHz). This property is also expected, as propagation is much less favorable for UEs at the cell edge at higher frequencies.

Fig. 4(b) shows the rate distribution with blockage. We observe that the cell edge rates at the high frequencies drop sharply. Indeed, UEs in 18 and 24 GHz show significantly worse performance approximately 35% of the time, compared to UEs in 6 and 12 GHz. Thus, when blockers, such as humans or vehicles, surround an UE, as would occur commonly in an urban scenario, the high-frequency coverage suffers significantly, while the low-frequency coverage is significantly more uniform.

The curves labeled "best choice" in Fig. 4(a) and Fig. 4(b) correspond to the rates for the UEs that select the best BS and frequency. As expected, the best choice is uniformly better than any individual frequency. Indeed, the best choice achieves the same peak rates as the UEs in the high-frequency bands, along with the improved cell edge rates of the low frequencies. These results motivate wideband cellular systems that adaptively select across a range of bands. Such systems can obtain the bandwidth benefits at high frequencies while providing robustness and resistance to blockage at low frequencies.

C. PENETRATION LOSS

In the previous section, we focused on outdoor UEs. Coverage for indoor from outdoor cell sites is called outdoor to indoor (O2I) penetration. To understand the potential for O2I coverage in the upper mid-band, Fig. 5 plots the 3GPP model [55, Table 7.4.3-1] for the loss of the O2I path for several common exterior building materials. For each material, the 3GPP model for pathloss is given by

$$L = a + bf \tag{2}$$

where L is the path loss in dB, f is the frequency in GHz, and a and b are linear constants that depend on the carrier frequency and are given in [55, Table 7.4.3-1]. Note that the curve in Fig. 5 does not appear linear since the pathloss is plotted on a logarithmic scale. We see that standard glass and wood are relatively permeable throughout the

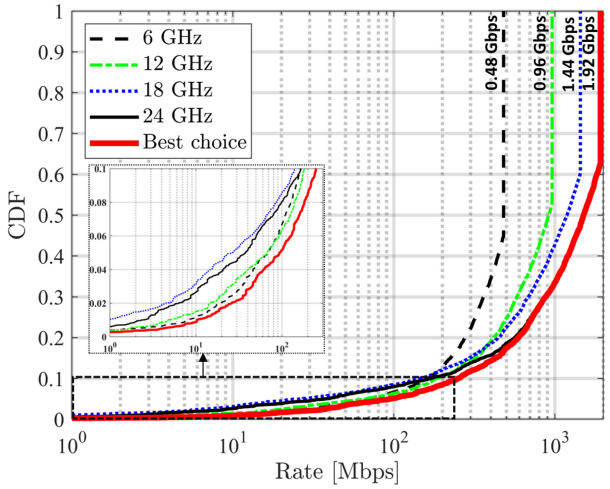

(a) Data rate CDF **without blockages**

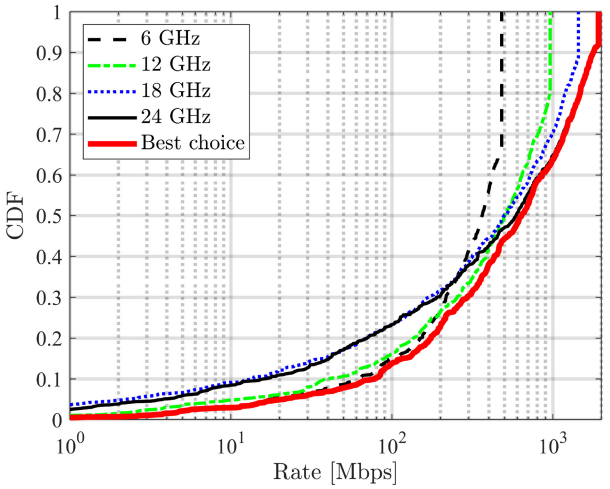

(b) Data rate CDF **with blockages**

FIGURE 4. **Aggregate multi-band rate distribution for all outdoor UEs.**

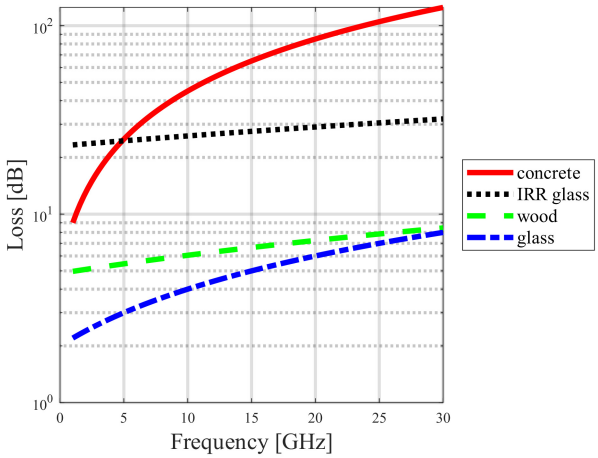

FIGURE 5. **3GPP model [55, Table 7.4.3-1] for outdoor-to-indoor penetration losses of various indoor materials at different frequencies.**

frequency range (<8 dB for both materials), while infrared reflecting glass (IRR) is relatively impermeable across all RF frequencies (>20 dB). Concrete, however, makes a sharp transition from relatively permeable to inpenetrable, precisely in the upper mid-band.

D. MULTIFREQUENCY INDOOR CAPACITY GAINS

To understand the effect of penetration loss on capacity, we re-run the simulation with users randomly placed indoors. Note that the 3D models used in the ray tracing have approximate material classifications for the facades of each building. Using the penetration loss models from Eq. (2) combined with the exterior wall classification, Fig. 6 plots the estimated CDFs of the SNR and data rate for *indoor* UEs. Fig. 6(a) shows that the SNR for indoor UEs is considerably reduced at higher frequencies due to high penetration loss, as mentioned in the previous section. In this setting, concrete is a dominant exterior wall material and significantly reduces the signal penetration – see Fig. 5. Indeed, Fig. 6(b) shows that, for roughly 65% of the users, the data rates at lower frequencies are higher than at higher frequencies. These results indicate a further potential gain of wideband cellular systems in FR3: the lower frequencies can provide valuable indoor coverage behind materials such as concrete while the higher frequencies can opportunistically offer high capacity for outdoor users and selected indoor users with minimal blockage (e.g., indoor users next to non-IRR glass windows).

E. EFFECTS OF INTERFERENCE

As the last discussion, we consider a full buffer interference scenario where BSs transmit data to their associated outdoor UEs simultaneously, and each UE receives interference signals from other BSs. Note that this is the worst-case scenario to show the lower bound of the system capacity gains. As before, considering 200 m ISD, 18 BSs are manually selected and concurrently transmit data to 18 UEs.

Fig. 7 shows the CDF of the signal-to-interference-noise ratio (SINR) and the corresponding data rate calculated using (1). As shown in Fig. 7(a), SINRs are degraded at lower frequencies (6 and 12 GHz) because the small number of antenna arrays produces wider beamwidths. In contrast, due to directional transmissions with narrow beamwidths, UEs at higher frequencies experience less interference.

As a result, we observe in Fig. 7(b) that data rates at higher frequency are almost uniformly better than those at lower frequency. Thus, the "best choice" always selects the high-frequency band. This result suggests yet another benefit of adaptive systems: in interference-limited scenarios, BSs or UEs can automatically choose bands where directionality can reduce interference.

Note that to clearly see the effect of interference, we have not added blocking in this simulation as we did earlier. If blocking were added, then the high frequency performance would degrade and not be uniformly better. The point is

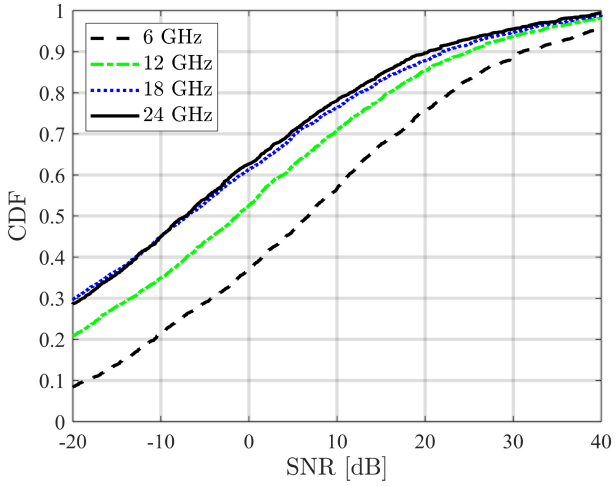

(a) SNR CDF

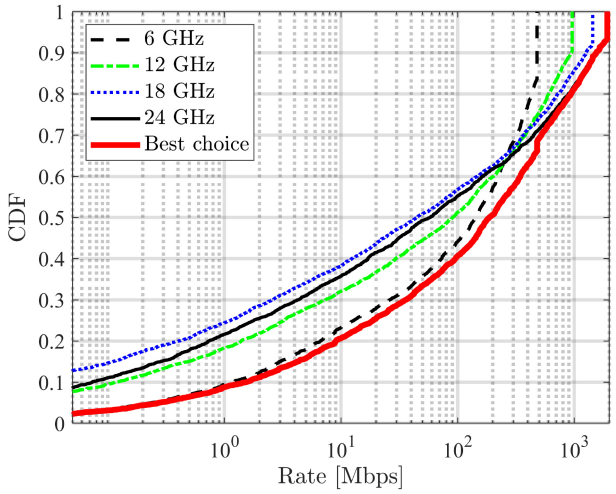

(b) Data rate CDF

FIGURE 6. Aggregate multi-band SNR and rate distribution for all indoor UEs.

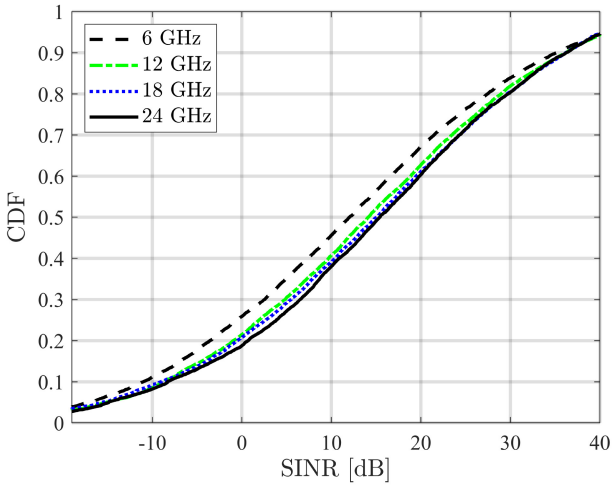

(a) SINR CDF

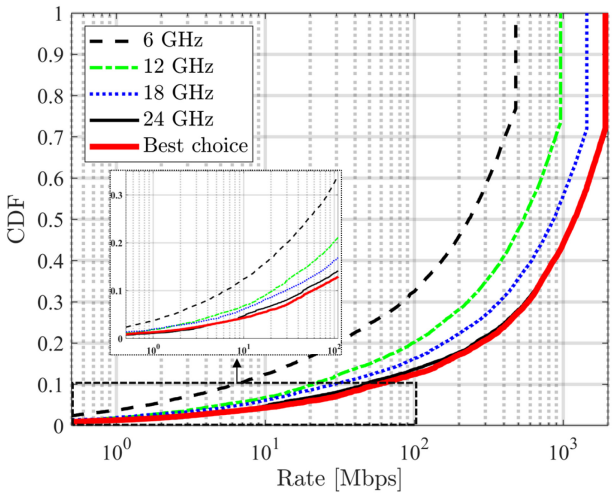

(b) Data rate CDF

FIGURE 7. Aggregate multi-band SINR and rate distribution for all outdoor UEs in a multi-cell setting with interference.

that adaptive systems can naturally select the optimal bands with multiple factors, including path loss, penetration, and directionality.

IV. INTERFERENCE WITH INCUMBENT SERVICES

A. COMMERCIAL COMMUNICATION SATELLITES

One of the most vital and growing incumbents in the upper mid-band are commercial communication satellites [57]. Fig. 8 shows the standard satellite bands. We see immediately that the X, Ku, and K bands – all widely used by satellites – fall entirely in the upper mid-band. In fact, recent FCC reports [19], [20] indicate extensive use of the bands by various commercial satellite services. Moreover, with the rapid growth of satellite Internet services, there is enormous demand for increased bandwidth, particularly in the 7-15 GHz bands. As an example, Fig. 8 shows the bands granted to the commercial satellite provider Starlink in the recent FCC grant [58]. As depicted, the bands in the grant are in both the uplink and downlink, as well as gateway-satellite and terminal-satellite links. 3GPP has also begun considering 5G NR services from satellites to mobile devices [59], [60], [61], including communication in the S, K, and Ka bands, which fall partly within the upper mid-band. More generally, satellite services are growing rapidly [62] and if terrestrial cellular services are to be deployed in significant fractions of the upper mid-band, co-existence with satellite services will be crucial.

B. ESTIMATING SATELLITE INTERFERENCE

Several recent works have analyzed interference between satellite and terrestrial networks. For example, [63] considers the selection of the network between satellite and terrestrial services. The works [64], [65] analyze interference of terrestrial networks onto the satellite downlink, i.e., satellite ground BSs, in the C-band. Similarly, [66] considers interference on the geostationary (GEO) and medium Earth orbit (MEO) satellite downlink in the Ka band. The work

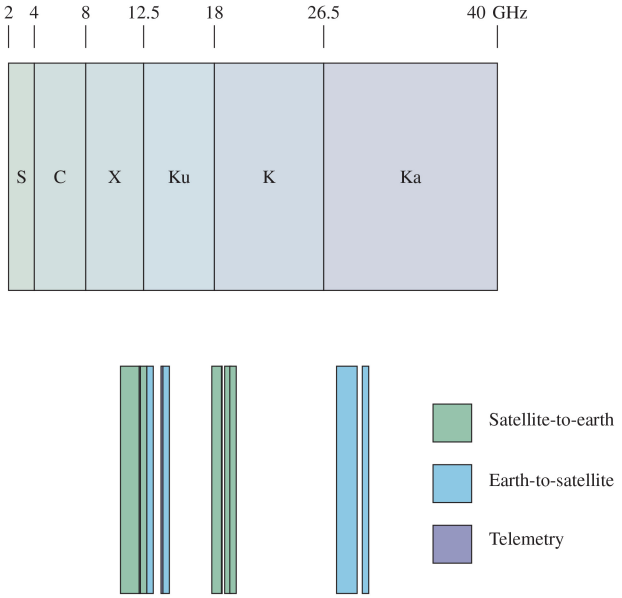

FIGURE 8. Top: Satellite bands. Bottom: Recent requests for the Starlink frequency band to the FCC [58]. Additional requests in the E-Band are not shown.

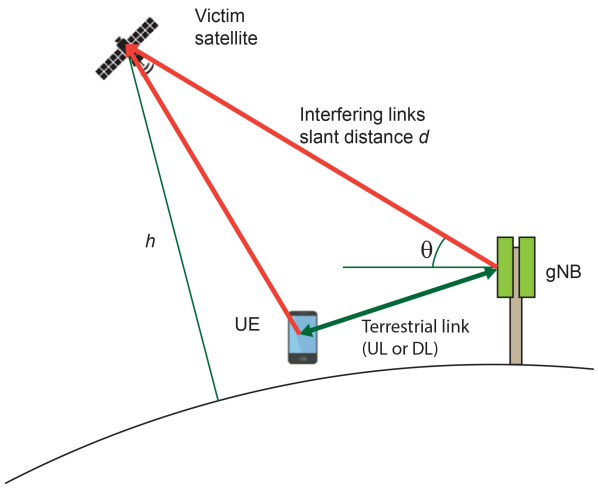

FIGURE 9. Terrestrial to satellite interference where terrestrial transmissions between a terrestrial gNB and UE interfere with the satellite uplink (UL).

[67] uses stochastic geometry to estimate interference in the satellite uplink, also in the Ka band.

In this work, we estimate the potential interference between terrestrial cellular networks and satellite services in the upper mid-band. As illustrated in Fig. 9, there exist possible interference channels to the low Earth orbit (LEO) satellite uplink by terrestrial networks. We will examine both the interference from the terrestrial downlink (DL, when the gNB is transmitting) and the terrestrial uplink (UL, when the UE is transmitting). When terrestrial UE or gNB transmits data, some portion of that signal energy is received as interference at a victim satellite. To obtain multipath channels for the DL and UL cases, we conducted an extensive ray tracing simulation. Based on the ray-tracing data, we build and run a simple system-level simulation to estimate the interference distribution.

TABLE 2. Terrestrial-satellite interference simulation parameters.

Parameters	Values
Carrier frequency f_c	$\{6, 18\}$ GHz
gNB transmit power P_{tx}	33 dBm
UE transmit power P_{tx}	23 dBm
Satellite transmission bandwidth, B	30 MHz
gNB TX array elevation orientation	12° downtilt
Satellite altitude h	600 km
Satellite elevation angle θ	Uniform in $[10°, 90°]$.
Satellite RX G/T	13 dB/K [60]
UE and gNB antenna pattern	3GPP TR 37.840 [50] with 65° horizontal and elevation half-power beam width, 30 dB front-to-back gain.
gNB antenna array	8×8 URA
UE antenna array	1×2 ULA
Additional propagation losses L_a (gaseous, cloud, fog, rain and scintillation)	0 dB

The system-level simulation parameters are listed in Table 2. Satellite altitude, h, and antenna gain-to-noise-temperature for satellites, G/T, are taken from [60, Sec. 6.1.1.1] for the Set-1 LEO-600 case in the Ka band. We presume that the peak gain is achievable in the entire simulation area, corresponding to the case where we are looking at a satellite beam focused in the simulation region. Interference in a victim satellite is calculated under the assumption that there is no additional attenuation L_a, except for pathloss provided by the ray-tracing simulation, to make the analysis conservative (including this attenuation will reduce interference). The antenna pattern for the gNB and UE are taken [50] with half-power beamwidths of 65° in both azimuth and elevation, maximum element gain of 8 dBi, and front-to-back gain of 30 dB.

We selected a typical rural area shown in Fig. 10 and examined a rural setting, as such areas are essential for satellite coverage. A satellite is placed at an altitude $h = 600$ km located at a random azimuth angle and an elevation angle θ uniformly distributed in $[10°, 90°]$. Note that the line-of-sight (LOS) distance to the satellite is the so-called *slant distance* given as

$$d(\theta) = \sqrt{R_E^2 \sin^2(\theta) + h^2 + 2hR_E} - R_E \sin(\theta) \qquad (3)$$

where R_E is the earth radius. A gNB and UE are randomly selected in the simulation area with the constraint that the UE is within 1 km of the BS.

We use ray-tracing data to estimate the multi-input multiple-output (MIMO) channel matrix, $\boldsymbol{H}_{\text{ter}}$, between the gNB and UE and the channel vector, $\boldsymbol{h}_{\text{sat}}$, from the gNB to the satellite for the DL case. In the UL case, $\boldsymbol{h}_{\text{sat}}$ is

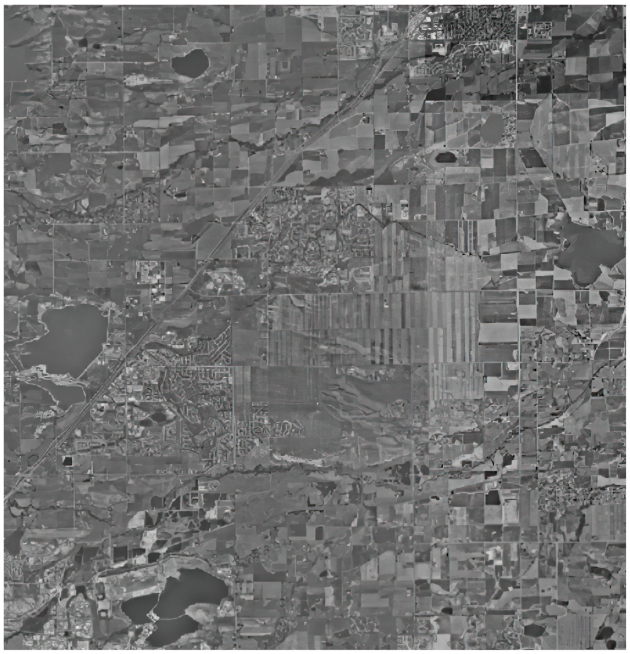

FIGURE 10. Colorado plains captured from ray-tracing simulator for satellite simulation in rural area.

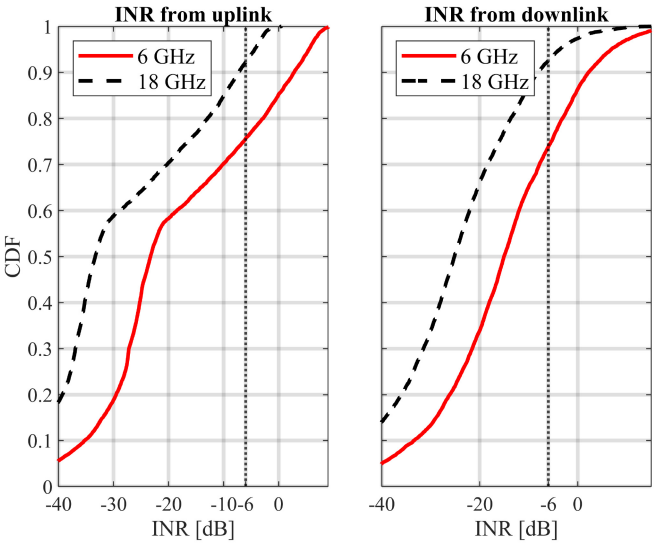

FIGURE 11. INR distribution from UL and DL terrestrial cellular sources.

the channel vector from the UE to the satellite. In both cases, as further discussed in the next section, $\boldsymbol{h}_{\text{sat}}$ can be approximately tracked using ephemeris data. For simplicity, we treat the satellite as a single antenna receiver, since the beamforming gain of the satellite is already incorporated into the G/T value. Furthermore, the channel matrices $\boldsymbol{H}_{\text{ter}}$ and $\boldsymbol{h}_{\text{sat}}$, include the gain of the antenna element for gNB or UE and the multipath components.

In our first simulation, we take into consideration the case where the terrestrial TX and RX select TX and RX beamforming vectors $\boldsymbol{w}_t$ and $\boldsymbol{w}_r$ to maximize the beamforming gain on the terrestrial link,

$$\widehat{\boldsymbol{w}}_t, \widehat{\boldsymbol{w}}_r = \arg\max_{\boldsymbol{w}_t, \boldsymbol{w}_r} \left| \boldsymbol{w}_r^{\mathsf{H}} \boldsymbol{H}_{\text{ter}} \boldsymbol{w}_t \right|^2 \tag{4}$$

where the optimization is solved over unit vectors. Assuming TX and RX perform channel estimation using pilot signals, the solution to (4) is given by the maximum singular vectors of $\boldsymbol{H}_{\text{ter}}$ [68].

Importantly, the selection of the beamforming vectors from (4) do not take into account the interference to the satellite uplink – it only maximizes the SNR on the terrestrial link. After taking the TX beamforming vector $\widehat{\boldsymbol{w}}_t$, the resulting channel from terrestrial TX to satellite RX will be $\widehat{\boldsymbol{w}}_t^{\mathsf{H}} \boldsymbol{h}_{\text{sat}}$. Hence, referencing the definition of carrier-to-noise ratio [59], the interference-to-noise ratio (INR) in dB at the satellite will be

$$\begin{aligned} \mathsf{INR} = {} & P_{\text{tx}} + 10\log_{10}\left| \widehat{\boldsymbol{w}}_t^{\mathsf{H}} \boldsymbol{h}_{\text{sat}} \right|^2 \\ & + \frac{G}{T} - L_a - 10\log_{10}(B) - 10\log_{10}(k) \end{aligned} \tag{5}$$

where P_{tx} is the total TX power of the UE or gNB, G/T is the satellite RX gain to thermal noise ratio in dB, L_a are the other propagation losses, B is the bandwidth, and k is Boltzmann's constant. Note that INR is a valuable metric for assessing the interference penalty in satellite services. Specifically, given an INR value, an intended uplink signal to the satellite will experience a degradation in SNR of

$$\Delta = 10\log_{10}\left(1 + 10^{0.1 \cdot \mathsf{INR}}\right) \tag{6}$$

Typical satellite systems require an $\mathsf{INR} < -6\,\text{dB}$ corresponding to an SNR degradation of $\Delta \approx 1\,\text{dB}$.

Plotted in Fig. 11 are the CDFs of the INR for both the uplink and downlink at two upper mid-band frequencies: $f_c = 6$ and $18\,\text{GHz}$. There are three important conclusions:

- *Possibility of high interference to the satellite uplink:* We see that the INR can be high. For example, at 6 GHz carrier frequency we see that approximately 27% of the downlink transmissions result in an $\mathsf{INR} \geq -6\,\text{dB}$, the level at which the satellite SNR degrades by more than $\Delta = 1\,\text{dB}$.
- *Both uplink and downlink terrestrial interference sources can be significant:* We see that the INRs can be large for transmissions by both the UE and the gNB. Although the UE transmits with a lower power, its antenna arrays can be in an arbitrary orientation. Therefore, with some probability, it can be oriented directly to the satellite. In the left panel of Fig. 11, we see that, even with terrestrial uplink transmissions, the $\mathsf{INR} > -6\,\text{dB}$ about 25% of the time when $f_c = 6\,\text{GHz}$. In contrast, the gNB is equipped with fixed downtilted antenna arrays. In such a case, the interference to the satellite uplink is caused by sidelobes occurring due to transmit beamforming of gNB.
- *Reduced interference at higher frequencies:* By Friis' law, the INRs are lower at higher frequencies. This property is considered to be useful for frequency adaptation to reduce interference to satellite services.

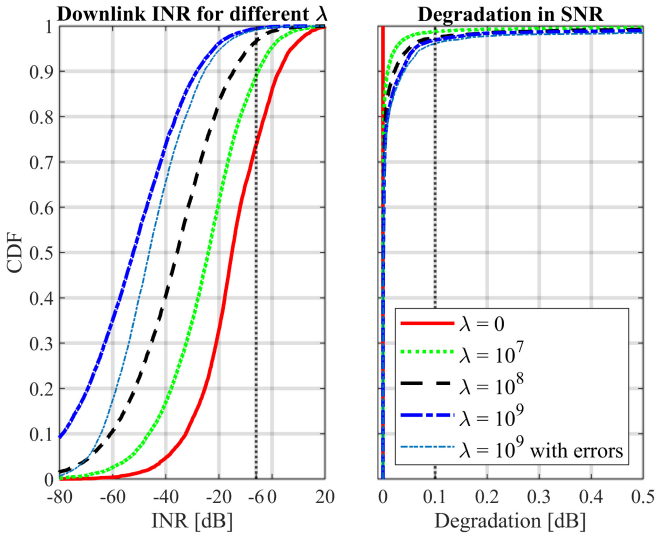

FIGURE 12. INR distribution from DL terrestrial cellular sources for different λ values at a carrier of 6 GHz.

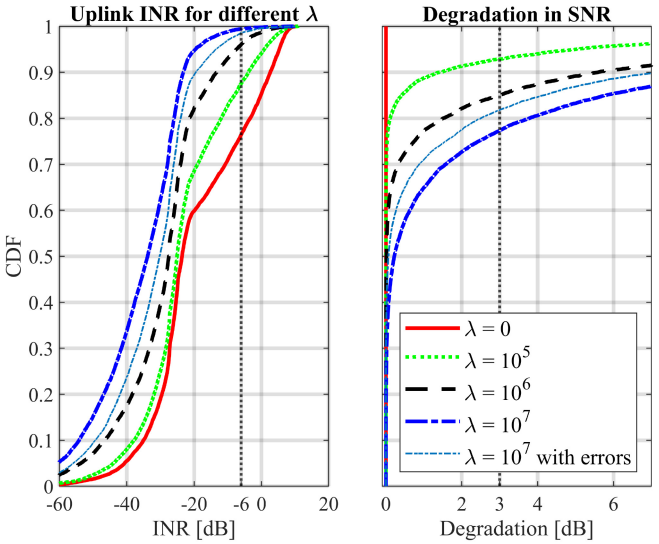

FIGURE 13. INR distribution from UL terrestrial cellular sources for different λ values at a carrier of 6 GHz.

C. REDUCING SATELLITE INTERFERENCE WITH NULLING

To mitigate the interference, the terrestrial transmitter can employ interference nulling as follows: Assume, for the time being, that the terrestrial transmitter knows the channel vector $\boldsymbol{h}_{\text{sat}}$ to the satellite along with the MIMO channel matrix $\boldsymbol{H}_{\text{ter}}$ between the gNB and the UE. We will discuss the estimate of the satellite channel vector in the next sub-section. As before, the receiver selects the beamforming vector $\widehat{\boldsymbol{w}}_r$ from (4). However, to eliminate interference, the transmitter selects a vector $\boldsymbol{w}_t$ via the regularized cost:

$$\widehat{\boldsymbol{w}}_t^{\lambda} = \arg\max_{\boldsymbol{w}_t} \left[\left| \boldsymbol{w}_r^{\mathsf{H}} \boldsymbol{H}_{\text{ter}} \boldsymbol{w}_t \right|^2 - \lambda \left| \boldsymbol{w}_t^{\mathsf{H}} \widehat{\boldsymbol{h}}_{\text{sat}} \right|^2 \right] \tag{7}$$

where $\lambda > 0$ is a regularization parameter. The regularization term, $|\boldsymbol{w}_t^{\mathsf{H}} \boldsymbol{h}_{\text{sat}}|^2$, penalizes the interference in the satellite receiver and attempts to create a null along the satellite channels. The solution $\widehat{\boldsymbol{w}}_t^{\lambda}$ to (7) is given by maximum eigenvector of

$$\boldsymbol{H}_{\mathsf{H}\text{ter}} \boldsymbol{w}_r \boldsymbol{w}_{r\mathsf{H}} \boldsymbol{H}_{\text{ter}} - \lambda \boldsymbol{h}_{\text{sat}} \boldsymbol{h}_{\mathsf{H}\text{sat}} \tag{8}$$

To assess the effectiveness of the nulling, we re-ran the identical simulation as in the previous subsection where the TX beamforming vector is computed from (8). We have considered the 6 GHz carrier frequency since the interference is higher in the lower band. The left panel of Fig. 12 plots the CDF of INR caused by terrestrial downlink transmissions to the satellite uplink at different values of λ. Regarding the curves labeled "with errors", we will discuss them in the next sub-section. From the left panel of Fig. 12, we see that with sufficiently high λ, the interference can be well mitigated, assuming ideal tracking. For example, when $\lambda = 10^8$, INR ≥ -6 dB less than 3% of the time.

Plotted on the right panel of Fig. 12 is the degradation in the SNR on the terrestrial link defined by

$$\rho = 10 \log_{10} \left(\frac{|\widehat{\boldsymbol{w}}_r \boldsymbol{H}_{\text{ter}} \widehat{\boldsymbol{w}}_t|^2}{|\widehat{\boldsymbol{w}}_r \boldsymbol{H}_{\text{ter}} \widehat{\boldsymbol{w}}_t^{\lambda}|^2} \right) \tag{9}$$

which is the ratio of the beamforming gain with the optimal beamforming vector $\widehat{\boldsymbol{w}}_t$ from (4) and the beamforming gain with the regularized beamforming vector $\widehat{\boldsymbol{w}}_t^{\lambda}$ from (7). We see that with a value of $\lambda = 10^8$, the degradation of the terrestrial SNR can be kept at ρ <0.1 dB for 97% of the time.

Fig. 13 similarly plots the CDF of the INR for terrestrial uplink transmission under different values λ along with the terrestrial degradation of the SNR ρ. We see here that the UEs can also reduce the interference, but the degradation is higher on the terrestrial link. We observe that the degradation of the SNR is less than 3 dB for 78% of time when $\lambda = 10^7$. This arises from the fact that the UE has a lower number of antennas, and hence directional nulling is more costly.

D. TRACKING INTERFERENCE CHANNELS TO SATELLITES

A practical issue with the above interference nulling method is that the UE and gNB must track the wideband channels to the satellite. Specifically, the cellular transmitter (UE or gNB) must estimate the channel $\boldsymbol{h}_{\text{sat}}$ at all frequencies. In this sub-section, we assess the possibility of using satellite *ephemeris data* to track azimuth and zenith angles of satellites. Ephemeris data are typically publicly available — see, for example, [69]. The use of these data has been considered by 3GPP [60].

To realistically assess the tracking with the ephemeris data, we need to take into account several practical challenges. First, knowing the satellite locations, one can only compute the LOS interference channels for victim satellites.

TABLE 3. Angular errors for tracking experiment.

Transmitter	Orientation device	RMS angle error	
		Azimuth	Elevation
gNB	High-precision compass, e.g. [70]	0.3°	0.1°
UE	3D magentometer with IMU and filtering, e.g. [71]	1.5°	1.5°

Therefore, we can use the ephemeris data to estimate the LOS component of the interference channel, ignoring the NLOS components. Since we are considering a rural scenario, the channels are dominated by LOS components, so considering only LOS interference channels should not significantly degrade performance. We will verify this assumption in the simulation below.

A second issue is the orientation calibration for ground antenna arrays. To use the ephemeris data, the orientation of the gNB or UE relative to the global frame must be known. For the gNB (base station), the orientation can be measured, for example, with a high-precision compass [70]. For the UE, the orientation can be measured with a magnetometer along with an inertial motion unit (IMU) and filtering techniques for tracking. These systems will introduce some angular error. Even if small, performance could be impacted, since spatial nulling tends to create very sharp nulls. To see this effect, we simulate the angular errors shown in Table 3 taken from the published measurements in [70], [71]. Specifically, we applied a random angular error given by the values in Table 3 to determine the estimated interference channels $\boldsymbol{h}_{\text{sat}}$ towards the victim satellites.

To better account for the angular errors, we modified the transmit beamforming procedure as the following

$$\widehat{\boldsymbol{w}}_t^{\lambda} = \arg\max_{\boldsymbol{w}_t} \left[\left| \boldsymbol{w}_r^{\mathsf{H}} \boldsymbol{H}_{\text{ter}} \boldsymbol{w}_t \right|^2 - \lambda \mathbb{E} \left| \boldsymbol{w}_t^{\mathsf{H}} \boldsymbol{h}_{\text{sat}} \right|^2 \right] \tag{10}$$

where $\boldsymbol{h}_{\text{sat}}$ includes only LOS component of interference channel to a satellite. The optimization is identical to (7) except for the regularization term $\mathbb{E}|\boldsymbol{w}_t^{\mathsf{H}} \boldsymbol{h}_{\text{sat}}|^2$. The expectation is taken over the distribution of channel vectors $\boldsymbol{h}_{\text{sat}}$ given the measured angular errors. This expectation encourages the creation of nulls, not just for the estimated angles of the satellites but rather for small regions around those angles to account for angular errors. The solution to (10) is described in a way similar to (8), but the expectation for $\boldsymbol{h}_{\text{sat}} \boldsymbol{h}_{\text{sat}}^{\mathsf{H}}$ should be taken over the distribution of the channel vectors $\boldsymbol{h}_{\text{sat}}$.

The final potential issues are variation of the tracked satellite location over the transmission time interval (TTI) and time synchronization. These time-related errors are, however, negligible. For example, since the TTI in 5G is generally less than 1 ms, and the velocity of a LEO satellite at an altitude of h =600 km is approximately $v = 7.56$ km/s, the maximum angular variation is at most $\Delta\theta = \tan^{-1}(vT/h) \approx 7.2 \times 10^{-4}$ degrees. This error is considerably less than the angular errors from the orientation calibration and can thus be neglected. The variation in tracked information due to synchronization errors in gNBs is also negligible, as network synchronization protocols such as the Precision Time Protocol (PTP) in the open radio access network (O-RAN) require nanosecond-scale timing synchronization errors [72].

Under these assumptions, we evaluate the modified interference nulling scheme given in (10) by running the same simulation as in the previous section. Fig. 12, shows the INR and gain loss CDFs with angular errors for the DL on the curve labeled "$\lambda = 10^9$ with errors". We see that the performance is almost identical to the curve without errors. Similarly, as shown in the curve labeled "$\lambda = 10^7$ with errors" of Fig. 13, we see that there is no significant change of INR due to angular errors for the UL case. Note that while tracking errors for UEs are assumed to be larger, as shown in Table 3, the effect of angular error is not as strong, as UEs have fewer antennas and produce less narrow nulls. Furthermore, since the nulls are created only on the LOS component, in the right panel of Fig. 12, we see the lower loss in SNR compared to the case without errors. For both gNB and UE, these results suggest that the modified interference nulling technique can work with reasonable tracking errors, even for high-speed LEO satellites.

E. RADIO ASTRONOMY

Radio astronomy studies the electromagnetic emissions from distant astronomical sources and high energy events [73], [74]. These emissions are wideband in nature, and reach the surface of the Earth strongly attenuated by their long-distance propagation throughout the interstellar or intergalactic media, but also due to atmospheric absorption.

Astronomical emissions can be characterized by their spectral shapes. They feature persistent continuum emissions depending on their nature [75], [76]: blackbody radiations for the cosmic background, free-free emissions, e.g., for star-forming regions, or synchrotron emissions, e.g., for neutron stars.

Gaseous or ionized sources also embed narrow features known as emission or absorption spectral lines [77], [78]. These lines are characteristics of the chemical elements present in the astronomical source, and are used to trace their composition, structure, and density. They are the only probes available to the interstellar medium and to external galaxies. They also reveal complementary information, such as gas temperatures, ionization, and fluid dynamics. More importantly, their shift in frequency from a given rest frequency, known as *redshift*, provides information on the age of the source and its distance to an observer. The International Astronomical Union (IAU) defined a list of the most important spectral lines, in which more than 25% fall in and below the mid-band (< 24 GHz). Notably, the complex prebiotic molecules, essential to the understanding of life processes in the Universe, have spectral signatures concentrated between 10 and 15 GHz [79], [80].

The spectral flux density of an astronomical sources is expressed in jansky (Jy), which is defined as $1\,\text{Jy} = 10^{-26}$ $\text{Wm}^{-2}\text{Hz}^{-1}$. To appreciate how small this flux density is, recall that an isotropic antenna at $f_c = 6\,\text{GHz}$ would have an aperture of $A = \lambda^2/(4\pi) \approx 2(10)^{-4}\,\text{m}^2$. A signal of 1 Jy with this antenna would thus be received at $-267\,\text{dBm}$, more than 90 dB below the noise floor. Observing milli- to micro-Jy sources are not uncommon with modern radio telescopes.

Detecting these weak emissions requires high sensitivity, which is achieved with radio telescopes using large collecting areas from wide reflectors or combined across multiple dish antennas, receivers with low system temperatures and wide bandwidths, and long integration times spanning seconds to hours of data integration.

Radio telescopes are also sensitive to Radio Frequency Interference (RFI), which can impact astronomical observations at various levels. Weak sources of RFI are detected after data integration in either or both time and frequency domains, and the associated corrupted time and frequency resource blocks are then discarded before further astronomical information extraction processes [81], [82]. The loss of data associated with this procedure not only reduces the sensitivity of an astronomical observation, which can possibly be recovered by longer observations, but may also prevent the observation of transient sources, such as Fast Radio Bursts [83] or counterparts of sources of gravitational waves, such as super massive black holes mergers [84], which are individual and non-repeatable events. Similarly, redshifted spectral lines can fall outside protected frequency bands where the astronomical information may be fully lost. This is for instance the case with the redshifted galactic Hydrogen line with rest frequency at 1400 MHz falling into the lower Global Navigation Satellite System (GNSS) bands (1145-1310 MHz), and preventing the observation of the edges of the local Universe [85]. Stronger sources of RFI can drive the electronics components of a telescope receiver into a nonlinear regime, leading to the complete loss of data loss.

The impact of RFI is minimized by locating radio observatories in remote areas with low population and terrestrial transmitter densities, exploiting the propagation losses of these transmissions due to their large distance from a radio observatory [86]. Further protection can be sought through coordination with active services to prevent the deployment of future radio frequency infrastructure, as is the case in the National Radio Quiet Zone (NRQZ) [87], [88]. Emerging work involving artificial intelligence (AI) and machine learning (ML) based nonlinear signal processing may help partially offset the effects of RFI from LEO constellations on radio astronomy [89].

V. WIDEBAND ANTENNAS FOR THE UPPER MID-BAND

A. CHALLENGES

The antennas and RF circuits of upper mid-band transceivers need to support wide bandwidths, high degree of tunability, and large numbers of antenna elements for directionality. Existing technologies have a number of bottlenecks in meeting these requirements including: a) antenna size-bandwidth-gain tradeoffs, 2) high frequency losses, 3) degraded SNR while scanning, 4) poor interference tolerance, and 5) inefficient spectrum management. To address the above shortfalls, here we combine a mix of wideband elements that are tunable and reconfigurable to mitigate interference and improve SNR across dynamically large spectrum swaths in the upper mid-bands.

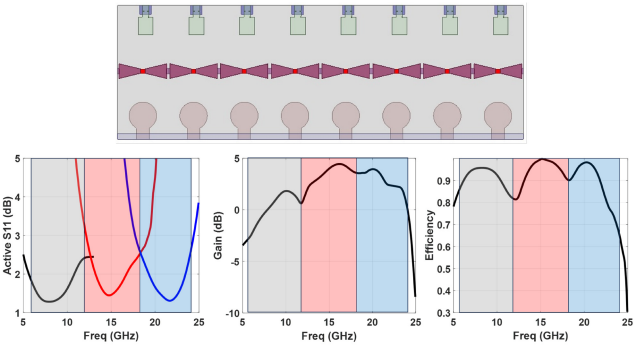

FIGURE 14. (Top) HFSS illustration of tri-band array, (Bottom) Simulated plots showing active VSWR, gain and efficiency of the array when all ports are excited.

Even though an antenna element can be designed to operate across the full range of interest, there are trade-offs that limit performance/ sensitivity and directional gain as a strong function of frequency if a single element is used in an array configuration for sensing applications. We want to avoid such compromises and trade-offs while covering the full band of interest, which requires several innovations in the antenna and microwave circuit areas for a cost-effective and scalable high-performance solution. Another key challenge in developing wideband systems for cellular applications is the antenna form factor. While there has been extensive work in wideband antennas (see, for example [90]), most designs require physically thick profiles that are not suitable for portable devices.

B. COMPACT WIDEBAND APERTURE IN APERTURE ANTENNA ARRAYS

To overcome the aforementioned challenge, a low-profile aperture-in-aperture (AiA) realization is investigated, considering 3 classes of antennas: a) ultra-wideband (UWB) tightly coupled arrays (TCDAs) [91], [92] [93], [94], [95], [96], b) low profile planar circular monopole [97], [98] [99], [100], [101], and c) UWB patches [102], [103], [104], [105]. Specifically, the unit cell of this array (see Fig. 14 was designed based on existing work in literature, which was later optimized to meet the requirements of the FR3 bands. Notably, the UWB performance offered by the TCDA is based on Wheeler's current sheet principle. In addition, the ground plane inductance is canceled using the capacitive overlaps of the dipoles, thereby eliminating unwanted resonances at certain frequency spots [93], [94].

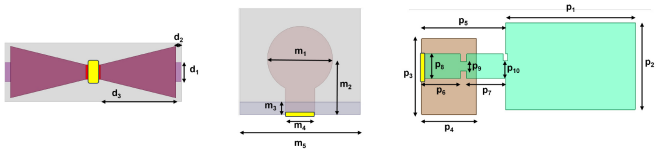

FIGURE 15. Dimensions of tri-band antennas. Excitation ports are depicted in yellow.

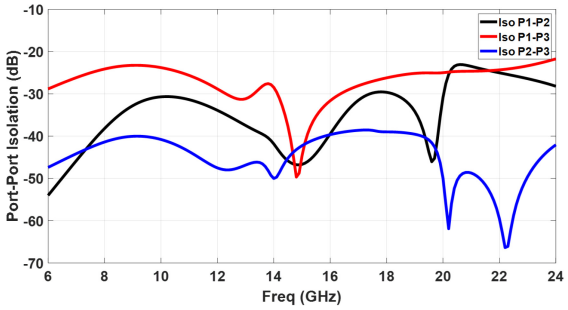

FIGURE 16. Port-port isolation exhibited by the co-located tri-band antennas. P1 corresponds to 6 - 12 GHz dipoles, P2 monopole spans 12 - 18 GHz, while P3 is represented by the patches operating across 18 - 24 GHz.

TABLE 4. Tri-band Antenna unit cell dimensions (in mm).

Dimension	Value [mm]	Dimension	Value [mm]
d_1	1.125	p_2	3
d_2	0.35	p_3	2.35
d_3	4.4	p_4	1.79
m_1	5.6	p_5	2.47
m_2	4.8	p_6	1.1
m_3	1.07	p_7	1
m_4	2.4	p_8	1.3
m_5	10.25	p_9	0.715
p_1	3.6	p_{10}	1.18

With the monopole, the ground plane, which serves as the counterpoise for the monopole, is designed to enhance the antenna's performance [99], [100], [101]. The size and shape of the ground plane play a role in determining the bandwidth. Similarly, by expanding the above approach, the bandwidth of the patch antenna was also increased. That is, the edges of the partial ground plane of the patch antenna were modified to allow for radiation, resulting in improving the impedance bandwidth of the patch antenna. Of course, this list is not exhaustive, and there are other types of wideband antennas that can also be considered. For instance, the holographic antennas can give the required bandwidth, as the holographic technique allows the use of sub-wavelength unit cells, and these reflectarrays and transmitarrays, such as [106], [107], [108], can be used in cellular network towers.

Notably, this AiA brings forward several unique features with game-changing impact in antenna array design and performance features. Specifically, they are: 1) scalable across all frequencies and geometries; 2) highly compact in terms of element size and thickness; 3) wide and continuous bandwidth of more than; 4) low-cost and easy to deploy in a highly conformal manner to mounted and deployed easily on any platform. Indeed, realizing low-cost fabrication and beamforming across wide bandwidths is one of the foundational challenges in our footsteps. The AiAs overcome this challenge quite effectively and with all the required characteristics rather naturally.

Unlike existing UWB arrays which use a single aperture for the entire band, here we present three separate antenna designs for each band. Doing so, provides the desired beam scanning across all the bands which is not the case with the former. Due to finite array size, using a single aperture significantly limits the beamscanning performance of the array due to the finite electrical array size at the lower bands. For instance, a typical 8×8 UWB array operating across a 4:1 impedance bandwidth, will have an antenna element spacing of $\lambda_{\text{high}}/2$. This corresponds to an inter-element spacing of $\lambda_{\text{low}}/8$ at the lowest band, implying that the effective number of elements at the lower band (6 GHz) is only 2. This significantly impacts the array scanning performance.

To address the above shortfall, a single aperture-in-aperture (AIA) antenna array comprising of 3 separate antenna arrays is designed. The lower band from $6-12$ GHz will comprise of closely spaced dipole arrays employing a co-axial feed, the mid-band from $12-18$ GHz will employ circular monopole, while the high-band from $18-24$ GHz will be realized using patches. The top panel of Fig. 14 depicts a simple illustration of the AiA geometry. The unit-cell dimensions are provided in Table 4. Notably, Ro4003 with permittivity ($\epsilon = 3.38$), loss tangent ($tan\delta = 0.0027$) was employed as a substrate with a thickness of 0.813 mm. The constant spacing between elements has been set to be 9 mm. Thus, the entire 8-element array measures 74 mm $\times$ 25 mm.

As depicted, a single aperture houses antennas operating across the entire upper mid-band band. The design optimization and simulation were performed using commercially available Ansys HFSS. The unit cell comprises of one antenna of each type with a semi-infinite boundary condition set-up. Hence, we used only 3 ports for our simulation depicted in yellow in Fig. 15. Active unit-element voltage standing wave ratio (VSWR), gain, and efficiency are provided in the bottom panel Fig. 14. As shown, all three antennas have a very good return loss or VWSR < 3. Further, the unit cell gain ranges from -2 to 4 dB across the operational FR3 bands. Finally, the average efficiency of this aperture is 82% with the upper bands experiencing a minimum efficiency of 67% at the upper ends. Fig. 16 provides the single element port-port isolation of the AIA. In Fig. 16, P1 corresponds to port-1 of the lower band antenna antenna radiating across 6 - 12 GHz. P2 corresponds to the midband antenna operating between 12 - 18 GHz, and P3 represents the ports of the patch antenna designed to operate between 18 - 24 GHz. As expected, the isolation between monopole (P2) and the patches(P3) is the maximum due

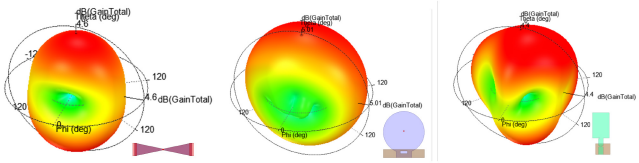

FIGURE 17. Unit cell radiation pattern at the center frequency of all 3 bands.

to their increased physical separation, in comparison to the placement of the dipoles. Nevertheless, the overall isolation or mutual coupling between the bands of AiA is still better than −18 dB. Finally, Fig. 17 shows the radiation pattern at the center frequencies of each band, specifically at 7.5 GHz, 15 GHz, and 21 GHz. It should be noted that the radiation pattern corresponds to a single antenna element within each band.

VI. OPEN RESEARCH PROBLEMS

The upper mid-band presents an enormous potential for cellular systems to deliver high data rates with consistent coverage and uniformity. Nevertheless, significant technical challenges remain to realize such systems. We summarize some open research problems indicated by the preliminary studies in this paper.

A. CHANNEL MEASUREMENTS AND CAPACITY ANALYSES

While there has been extensive channel measurements in the upper mid-band, certain aspects need further study. Most importantly, most of the measurement campaigns described in Section III-A captured the omni-directional path loss. Phased array systems, similar to those now widely-used in mmWave bands, could provide insights into the spatial structure of the channel which will be necessary for modeling MIMO and beamforming. The dynamics of blockage, across the band, will also need to be investigated, given how challenging blockage has been for mmWave systems.

Also, our study in Section III-B suggested the possibility of significant gains with wideband adaptive systems operating across the upper mid-band. However, the study was limited to a single urban area with only outdoor users. To analyze how general these results are, statistical models and more data, validated through measurements, will be needed. Current statistical models, such as those used by 3GPP [55], will also need to be extended. Large-scale statistical dependencies between multiple bands are not well modeled, and data-driven techniques, such as those recently proposed in [109] may be valuable.

B. INTERFERENCE WITH INCUMBENTS

Similarly, our analysis in Section IV-B suggested that high density LEO constellations can be susceptible to interference from terrestrial cellular services, but spatial nulling may be able to mitigate these effects. Further research, however, is required. Interference nulling will require tracking, including tracking of NLOS components, such as ground reflections, which can be significant when one wants to suppress interference by more than 20 dB. Protocols that can also selectively avoid the time and frequency of transmissions that cannot be mitigated will also be needed. Further work will be needed for other constellations as well as interference with radio astronomy and other passive sources, which we have only briefly mentioned.

C. ANTENNAS AND CIRCUITS

The design presented in Section V indicates the possibility of a compact multiband antenna structure that can cover the entire wideband with appropriate RF switching. One limitation in the current design is that the elements are assumed to be probe fed and further work will be needed to build microstrip fed structures and packaging to realize such antennas in practical devices. In addition, tightly coupled arrays require signal processing to account for the mutual coupling at lower bands. In addition, we have not addressed the design of the RF circuits and switches that will need to operate across a wideband with a large number of antenna elements.

D. SECURITY AND RESILIENCY

Due to space considerations, this article has not touched on the vital topic of security, a key area mentioned in the FCC study [20]. Spectrally agile systems in the upper mid-band could provide new resiliency to hostile attacks by sensing signals and frequency hopping. There is broad literature on such systems, but little has been researched specifically in the context of cellular multi-band systems. Furthermore, we have seen that satellite signals can be significantly impacted by low-power random terrestrial signals at these frequencies. This fact suggests that an adversarial attacker could significantly disrupt vital LEO satellite services. Methods to detect and mitigate such attacks, possibly leveraging terrestrial measurements, will be an area of paramount importance.

VII. CONCLUSION

We have provided a detailed assessment of both the potential benefits and challenges that may arise for cellular use in the upper-mid band. This analysis yields valuable insights:

Capacity gains: The potential capacity gains of a wideband FR3 was assessed in an urban scenario. As expected, we showed that the overall system capacity was maximized when lower frequencies are dedicated to cell edge users, due to the more favorable propagation features. Similarly, such frequencies are indispensable for indoor UEs, owing to the substantial penetration losses in higher frequencies introduced by materials such as walls and glass. On the other hand, the key benefits of the higher frequencies stem from (1) the availability of high bandwidths and (2) the intrinsic directionality, and hence interference isolation, which translate in higher data rates. These results demonstrate the value of systems that can dynamically select frequency across the upper mid-band.

Coexistence: Then, we analyze the coexistence between cellular services and satellite incumbents, and conclude that interference may lead to substantial degradation in the performance of satellite networks. For this reason, we propose an interference nulling scheme that enables terrestrial networks to significantly reduce that interference.

Antenna design: A compact wide-band antenna array is presented based on a low-profile aperture-in-aperture (AiA) realization and three classes of antennas (coupled dipole array, circular monopole, and UWB patches). The presented aperture provides contiguous coverage across the entire FR3 bands.

ACKNOWLEDGMENT

The authors would like to thank Muhammad Mubasshir Hossain for his assistance with the antenna design and the CAD tool.

REFERENCES

[1] E. Dahlman, S. Parkvall, and J. Skold, *5G NR: The Next Generation Wireless Access Technology*. Cambridge, MA, USA: Academic, 2020.

[2] *NR; Overall Description; Stage-2*, 3GPP Standard TS 38.300, 2020.

[3] S. Rangan, T. S. Rappaport, and E. Erkip, "Millimeter-wave cellular wireless networks: Potentials and challenges," *Proc. IEEE*, vol. 102, no. 3, pp. 366–385, Mar. 2014.

[4] M. Akdeniz et al., "Millimeter wave channel modeling and cellular capacity evaluation," *IEEE J. Sel. Areas Commun.*, vol. 32, no. 6, pp. 1164–1179, Jun. 2014.

[5] M. Shafi et al., "5G: A tutorial overview of standards, trials, challenges, deployment, and practice," *IEEE J. Sel. Areas Commun.*, vol. 35, no. 6, pp. 1201–1221, Jun. 2017.

[6] A. Narayanan et al., "A variegated look at 5G in the wild: Performance, power, and QoE implications," in *Proc. ACM SIGCOMM Conf.*, 2021, pp. 610–625.

[7] C. Wei, A. Kak, N. Choi, and T. Wood, "5GPerf: Profiling open source 5G RAN components under different architectural deployments," in *Proc. ACM SIGCOMM Workshop 5G Beyond Netw. Meas., Model., Use Cases*, 2022, pp. 43–49.

[8] A. Narayanan et al., "A comparative measurement study of commercial 5G mmWave deployments," in *Proc. IEEE INFOCOM Conf. Comput. Commun.*, 2022, pp. 800–809.

[9] M. I. Rochman et al., "A comparison study of cellular deployments in Chicago and Miami using Apps on smartphones," in *Proc. 15th ACM Workshop Wireless Netw. Testbeds, Exp. Eval. Characterization*, 2022, pp. 61–68.

[10] T. S. Rappaport, R. W. Heath Jr., R. C. Daniels, and J. N. Murdock, *Millimeter Wave Wireless Communications*. London, U.K.: Pearson Educ., 2014.

[11] C. Slezak, V. Semkin, S. Andreev, Y. Koucheryavy, and S. Rangan, "Empirical effects of dynamic human-body blockage in 60 GHz communications," *IEEE Commun. Mag.*, vol. 56, no. 12, pp. 60–66, Dec. 2018.

[12] C. Slezak, M. Zhang, M. Mezzavilla, and S. Rangan, "Understanding end-to-end effects of channel dynamics in millimeter wave 5G new radio," in *Proc. IEEE Int. Workshop Signal Process. Adv. Wireless Commun. (SPAWC)*, 2018, pp. 1–5.

[13] G. R. MacCartney, T. S. Rappaport, and S. Rangan, "Rapid fading due to human blockage in pedestrian crowds at 5G millimeter-wave frequencies," in *Proc. IEEE Global Commun. Conf.*, 2017, pp. 1–7.

[14] A. B. Zekri, R. Ajgou, A. Chemsa, and S. Ghendir, "Analysis of outdoor to indoor penetration loss for mmWave channels," in *Proc. 1st Int. Conf. Commun., Control Syst. Signal Process. (CCSSP)*, 2020, pp. 74–79.

[15] J. Smee. "Ten innovation areas for 5G advanced and beyond [video]." QnQ Blog. 2022. [Online]. Available: https://www.qualcomm.com/news/onq/2022/02/10-innovation-areas5g-advanced-and-beyond

[16] "6G spectrum: Expanding the frontier." Samsung. 2022. [Online]. Available: https://cdn.codeground.org/nsr/downloads/researchareas/2022May_6G_Spectrum.pdf

[17] "Becoming 5G-advanced: The 3GPP 2025 roadmap," 5G Americas, Bellevue, WA, USA, White Paper, 2022. [Online]. Available: https://www.5gamericas.org/wp-content/uploads/2022/12/Becoming-5G-Advanced-the-3GPP-2025-Roadmap-InDesign.pdf,

[18] K. Lee, J. Kim, E. W. Jin, and K. S. Kim, "Extreme massive MIMO for upper-mid band 6G communications," in *Proc. 13th Int. Conf. Inf. Commun. Technol. Converg. (ICTC)*, 2022, pp. 997–999.

[19] "A preliminary view of spectrum bands in the 7.125–24 GHz range; and a summary of spectrum sharing frameworks," FCC Technical Advisory Council, Aug. 2023. [Online]. Available: https://www.fcc.gov/sites/default/files/SpectrumSharingReportforTAC

[20] "6G working group position paper," FCC Technical Advisory Council, Aug. 2023. [Online]. Available: https://www.fcc.gov/sites/default/files/Consolidated_6G_Paper_FCCTAC23_Final_for_Web.pdf

[21] *Study on the 7 to 24 GHz Frequency Range for NR*, 3GPP Standard TS 38.820, 2020.

[22] V. Sathya, S. M. Kala, M. I. Rochman, M. Ghosh, and S. Roy, "Standardization advances for cellular and wi-Fi coexistence in the unlicensed 5 and 6 GHz bands," *GetMobile Mobile Comput. Commun.*, vol. 24, no. 1, pp. 5–15, 2020.

[23] S. Akoum, O. El Ayach, and R. W. Heath, "Coverage and capacity in mmWave cellular systems," in *Proc. Conf. Rec. 46th Asilomar Conf. Signals, Syst. Comput. (ASILOMAR)*, 2012, pp. 688–692.

[24] T. S. Rappaport et al., "Millimeter wave mobile communications for 5G cellular: It will work!" *IEEE Access*, vol. 1, pp. 335–349, 2013.

[25] "3.5 GHz band overview," FCC, 2023. [Online]. Available: https://www.fcc.gov/wireless/bureau-divisions/mobility-division/35-ghz-band/35-ghz-band-overview

[26] "Report and order. order proposing modification: In the matter of expanding flexible use in the 3.7-4.2 GHz band," FCC, Washington, DC, USA, document Docket 18-122, FCC-20-22, 2022.

[27] A. Aijaz, "Private 5G: The future of industrial wireless," *IEEE Ind. Electron. Mag.*, vol. 14, no. 4, pp. 136–145, Dec. 2020.

[28] *IEEE Standard for Information Technology—Telecommunications and Information Exchange Between Systems—Local and Metropolitan Area Networks—Specific Requirements—Part 11: Wireless LAN Medium Access Control (MAC) and Physical Layer (PHY) Specifications—Amendment 1: Enhancements for High-Efficiency WLA*, IEEE Standard 802.11ax, 2021. [Online]. Available: https://standards.ieee.org/ieee/802.11ax/7180/

[29] G. Naik and J.-M. J. Park, "Coexistence of Wi-Fi 6E and 5G NR-U: Can we do better in the 6 GHz bands?" in *Proc. IEEE INFOCOM Conf. Comput. Commun.*, 2021, pp. 1–10.

[30] S. Kechiche. "mmWave clocks gigabit speeds in the U.S. but lacks maturity elsewhere." Ookla. Feb. 2023. [Online]. Available: https://www.ookla.com/articles/mmwave-spectrum-gigabit-speeds-us-q1-2023

[31] F. Rizzato. "Quantifying the mmWave 5G experience in the U.S." OpenSignal. Apr. 2021. [Online]. Available: https://www.opensignal.com/2021/04/28/quantifying-the-mmwave-5g-experience-in-the-us

[32] *Study on International Mobile Telecommunications (IMT) Parameters for 6.425–7.025 GHz, 7.025–7.125 GHz and 10.0–10.5 GHz*, 3GPP Standard TS 38.921, 2022.

[33] "Notice of proposed rulemaking: Expanding flexible use of the 12.2-12.7 GHz band," FCC, Washington, DC, USA, document Docket 20-443, FCC-21-13, 2021.

[34] "Notice of inquiry and order: Expanding use of the 12.7-13.25 GHz band for mobile broadband or other expanded use," FCC, Washington, DC, USA, document Docket 22-352, FCC 22-80, 2022.

[35] M. D. Mueck, S. Srikanteswara, and B. Badic, "Spectrum sharing: Licensed shared access (LSA) and spectrum access system (SAS)," Intel, Santa Clara, CA, USA, White Paper, pp. 1–26, 2015.

[36] M. Matinmikko-Blue, S. Yrjölä, and P. Ahokangas, "Spectrum management in the 6G era: The role of regulation and spectrum sharing," in *Proc. 2nd 6G Wireless Summit (6G SUMMIT)*, 2020, pp. 1–5.

[37] "Release 17 description; summary of Rel-17 work items," 3GPP, Sophia Antipolis, France, Rep. TR 21.917, 2022.

[38] "What can we do with 5G NR spectrum sharing that isn't possible today?" Qualcomm. 2017. [Online]. Available: https://www.qualcomm.com/content/dam/qcomm-martech/dm-assets/documents/nrss_webinar_dec_2017_v8.2_final.pdf

[39] "GeoPipe." [Online]. Available: https://https://www.geopipe.ai//

[40] G. J. Janssen and R. Prasad, "Propagation measurements in an indoor radio environment at 2.4 GHz, 4.75 GHz and 11.5 GHz," in *Proc. Veh. Technol. Soc. 42nd VTS Conf.-Front. Technol.*, 1992, pp. 617–620.

[41] G. J. Janssen, P. A. Stigter, and R. Prasad, "Wideband indoor channel measurements and BER analysis of frequency selective multipath channels at 2.4, 4.75, and 11.5 GHz," *IEEE Trans. Commun.*, vol. 44, no. 10, pp. 1272–1288, Oct. 1996.

[42] Y. L. De Jong, J. A. Pugh, M. Bennai, and P. Bouchard, "2.4 to 61 GHz multiband double-directional propagation measurements in indoor office environments," *IEEE Trans. Antennas Propag.*, vol. 66, no. 9, pp. 4806–4820, Sep. 2018.

[43] I. D. S. Batalha et al., "Indoor corridor and office propagation measurements and channel models at 8, 9, 10 and 11 GHz," *IEEE Access*, vol. 7, pp. 55005–55021, 2019.

[44] S. Deng, G. R. MacCartney, and T. S. Rappaport, "Indoor and outdoor 5G diffraction measurements and models at 10, 20, and 26 GHz," in *Proc. IEEE Global Commun. Conf. (GLOBECOM)*, 2016, pp. 1–7.

[45] I. Rodriguez, H. C. Nguyen, N. T. Jorgensen, T. B. Sorensen, and P. Mogensen, "Radio propagation into modern buildings: Attenuation measurements in the range from 800 MHz to 18 GHz," in *Proc. IEEE 80th Veh. Technol. Conf. (VTC-Fall)*, 2014, pp. 1–5.

[46] V. Kristem, C. U. Bas, R. Wang, and A. F. Molisch, "Outdoor wideband channel measurements and modeling in the 3–18 GHz band," *IEEE Trans. Wireless Commun.*, vol. 17, no. 7, pp. 4620–4633, Jul. 2018.

[47] H. Miao et al., "Sub-6 GHz to mmWave for 5G-advanced and beyond: Channel measurements, characteristics and impact on system performance," *IEEE J. Sel. Areas Commun.*, vol. 41, no. 6, pp. 1945–1960, Jun. 2023.

[48] Q. Pan, G. H. Bryant, J. McMahon, J. E. Allnutt, and F. Haidara, "High elevation angle satellite-to-earth 12 GHz propagation measurements in the tropics," *Int. J. Satell. Commun.*, vol. 19, no. 4, pp. 363–384, 2001.

[49] "Base station (BS) conformance testing part 2: Radiated conformance testing," 3GPP, Sophia Antipolis, France, Rep. TR 38.141-2, 2020.

[50] *Study of Radio Frequency (RF) and Electromagnetic Compatibility (EMC) Requirements for Active Antenna Array System (AAS) Base Station*, 3GPP Standard TS 37.840, 2014.

[51] I. K. Jain, R. Kumar, and S. Panwar, "Driven by capacity or blockage? A millimeter wave blockage analysis," in *Proc. 30th Int. Teletraffic Congr. (ITC)*, vol. 1, 2018, pp. 153–159.

[52] "Electromagnetic simulation software: Solutions for design engineers and EM simulation professionals." Remcom. 2024. [Online]. Available: https://www.remcom.com/

[53] Y. de Jong et al., "Ray-optical modeling of wireless coverage enhancement using engineered electromagnetic surfaces: Experimental verification at 28 GHz," in *Proc. 53rd Eur. Microw. Conf. (EuMC)*, 2023, pp. 702–705.

[54] P. Vigneron. "Millimetre waves: Modelling and simulation to engineer for coverage." Aug. 2017. [Online]. Available: https://its.ntia.gov/media/66446/vigneron_isart2017.pdf

[55] "Study on channel model for frequency spectrum from 0.5 to 100 GHz," 3GPP, Sophia Antipolis, France, Rep. TR 38.901, 2020.

[56] P. Mogensen et al., "LTE capacity compared to the Shannon bound," in *Proc. IEEE 65th Veh. Technol. Conf.*, 2007, pp. 1234–1238.

[57] J. Huang and J. Cao, "Recent development of commercial satellite communications systems," in *Proc. Artif. Intell. China Proc. Int. Conf. Artif. Intell. China*, 2020, pp. 531–536.

[58] (FCC, Washington, DC, USA). *FCC-22-91A1: Order and Authorization in Matter of Space Exploration Holdings, LLC Request for Orbital Deployment and Operating Authority for the SpaceX Gen2 NGSO Satellite System*. (Nov. 2022). [Online]. Available: https://docs.fcc.gov/public/attachments/FCC-22-91A1.pdf

[59] "Study on new radio (NR) to support non-terrestrial networks," 3GPP, Sophia Antipolis, France, Rep. TR 38.811, 2018.

[60] "Solutions for NR to support non-terrestrial networks (NTN)," 3GPP, Sophia Antipolis, France, Rep. TR 38.821, 2019.

[61] X. Lin, S. Rommer, S. Euler, E. A. Yavuz, and R. S. Karlsson, "5G from space: An overview of 3GPP non-terrestrial networks," *IEEE Commun. Stand. Mag.*, vol. 5, no. 4, pp. 147–153, Dec. 2021.

[62] "Satellite Internet market size, share & trends analysis report by frequency band (L-band, C-band, K-band, and X-band), by industry, by region (North America, Europe, Asia Pacific, Latin America, MEA), and segment forecasts, 2023–2030." Grand View Research. 2023. [Online]. Available: https://www.grandviewresearch.com/industry-analysis/satellite-internet-market-report

[63] P. K. Sharma, P. K. Upadhyay, D. B. da Costa, P. S. Bithas, and A. G. Kanatas, "Performance analysis of overlay spectrum sharing in hybrid satellite-terrestrial systems with secondary network selection," *IEEE Trans. Wireless Commun.*, vol. 16, no. 10, pp. 6586–6601, Oct. 2017.

[64] G. Hattab, P. Moorut, E. Visotsky, M. Cudak, and A. Ghosh, "Interference analysis of the coexistence of 5G cellular networks with satellite earth stations in 3.7-4.2 GHz," in *Proc. IEEE Int. Conf. Commun. Workshops (ICC Workshops)*, 2018, pp. 1–6.

[65] E. Lagunas, C. G. Tsinos, S. K. Sharma, and S. Chatzinotas, "5G cellular and fixed satellite service spectrum coexistence in C-band," *IEEE Access*, vol. 8, pp. 72078–72094, 2020.

[66] C. Zhang, C. Jiang, L. Kuang, J. Jin, Y. He, and Z. Han, "Spatial spectrum sharing for satellite and terrestrial communication networks," *IEEE Trans. Aerosp. Electron. Syst.*, vol. 55, no. 3, pp. 1075–1089, Jun. 2019.

[67] A. Yastrebova et al., "Theoretical and simulation-based analysis of terrestrial interference to LEO satellite uplinks," in *Proc. IEEE Global Commun. Conf.*, 2020, pp. 1–6.

[68] R. W. Heath Jr. and A. Lozano, *Foundations of MIMO Communication*. Cambridge, U.K.: Cambridge Univ. Press, 2018.

[69] "Celestrack." [Online]. Available: https://celestrak.org/

[70] "EC2000 high accuracy 3D electronic compass," 2019. [Online]. Available: https://www.skymems.com/products/ec2000-high-accuracy-3d-electronic-compass/

[71] W. Teufl, M. Miezal, B. Taetz, M. Fröhlich, and G. Bleser, "Validity, test-retest reliability and long-term stability of magnetometer free inertial sensor based 3D joint kinematics," *Sensors*, vol. 18, no. 7, p. 1980, 2018.

[72] *Publicly Available Specification (PAS); O-RAN Fronthaul Control, User and Synchronization Plane Specification V07.02*, 3GPP Standard TS 103.859, 2022.

[73] J. J. Condon and S. M. Ransom, *Essential Radio Astronomy*, vol. 2. Princeton, NJ, USA: Princeton Univ. Press, 2016.

[74] B. F. Burke, F. Graham-Smith, and P. N. Wilkinson, *An Introduction to Radio Astronomy*. Cambridge, U.K.: Cambridge Univ. Press, 2019.

[75] *Spectrum Management for Science in the 21st Century*. Washington, DC, USA: Nat. Acad. Press, 2010.

[76] N. R. Council et al., *Handbook of Frequency Allocations and Spectrum Protection for Scientific Uses*. Washington, DC, USA: Nat. Acad. Press, 2007.

[77] K. Rohlfs and T. L. Wilson, *Tools of Radio Astronomy*. Cham, Switzerland: Springer, 2013.

[78] A. Barrett, "Spectral lines in radio astronomy," *Proc. IRE*, vol. 46, no. 1, pp. 250–259, Jan. 1958.

[79] P. Thaddeus, "The prebiotic molecules observed in the interstellar gas," *Philosoph. Trans. Royal Soc. B, Biol. Sci.*, vol. 361, no. 1474, pp. 1681–1687, 2006.

[80] J. Corby, "Astrochemistry in the age of broadband radio astronomy," Ph.D. dissertation, Dept. Astronomy, Charlottesville, VA, USA, 2016.

[81] W. A. Baan, "RFI mitigation in radio astronomy," in *Proc. XXXth URSI General Assem. Sci. Symp.*, 2011, pp. 1–2.

[82] J. M. Ford and K. D. Buch, "RFI mitigation techniques in radio astronomy," in *Proc. IEEE Geosci. Remote Sens. Symp.*, 2014, pp. 231–234.

[83] E. Petroff, J. Hessels, and D. Lorimer, "Fast radio bursts," *Astron. Astrophys. Rev.*, vol. 27, pp. 1–75, 2019.

[84] K. Hotokezaka, S. Nissanke, G. Hallinan, T. J. W. Lazio, E. Nakar, and T. Piran, "Radio counterparts of compact binary mergers detectable in gravitational waves: A simulation for an optimized survey," *Astrophys. J.*, vol. 831, no. 2, p. 190, 2016.

[85] A. Gilloire and H. Sizun, "RFI mitigation of GNSS signals for radio astronomy: Problems and current techniques," *Ann. Telecommun. Annales des TéléCommun.*, vol. 64, pp. 625–638, Jun. 2009.

[86] R. Umar, Z. Z. Abidin, and Z. A. Ibrahim, "The importance of site selection for radio astronomy," in *Proc. J. Phys. Conf. Ser.*, vol. 539, 2014, Art. no. 12009.
[87] W. Sizemore and J. Acree, *The National Radio Quiet Zone*, Emerson, St. Louis, MO, USA, p. 217, 2002.
[88] "Characteristics of radio quiet zones," Int. Telecommun. Union, Geneva, Switzerland, Rep. ITU-R RA.2259-1, 2021.
[89] A. Madanayake, S. Venkatakrishnan, U. De Silva, G. Hellbourg, J. Volakis, and T. Rappaport, "AI/ML intereference cancellation used in STAR wireless for radio astronomy RFI control," presented at IEEE Int. Conf. Microw., Commun., Antennas, Biomed. Eng. Electron. Syst. (COMCAS), 2023.
[90] E. G. Lim, Z. Wang, C.-U. Lei, Y. Wang, and K. Man, "Ultra wideband antennas: Past and present," *IAENG Int. J. Comput. Sci.*, to be published.
[91] A. D. Johnson, S. B. Venkatakrishnan, E. A. Alwan, and J. L. Volakis, "Balanced wideband impedance transformer (BWIT) for common-mode resonance cancellation in UWB dipoles over a ground plane," in *Proc. Int. Appl. Comput. Electromagnetics Soc. Symp. (ACES)*, 2020, pp. 1–2.
[92] A. D. Johnson, V. Manohar, S. B. Venkatakrishnan, and J. L. Volakis, "Optimized differential TCDA (D-TCDA) with novel differential feed structure," *IEEE Open J. Antennas Propag.*, vol. 2, pp. 464–472, 2021.
[93] J. P. Doane, K. E. Kolodziej, and B. T. Perry, "Simultaneous transmit and receive with digital phased arrays," in *Proc. IEEE Int. Symp. Phased Array Syst. Technol. (PAST)*, Oct. 2016, pp. 1–6.
[94] A. D. Johnson, S. B. Venkatakrishnan, E. A. Alwan, and J. L. Volakis, "Suppressing E-plane scan resonance for UWB Millimeter-wave differential phased array," in *Proc. Int. Appl. Comput. Electromagn. Soc. Symp. (ACES)*, Apr. 2019, pp. 1–2.
[95] I. Tzanidis, K. Sertel, and J. Volakis, "UWB low-profile tightly coupled dipole array with integrated balun and edge terminations," *IEEE Trans. Antenna Propag.*, vol. 61, no. 6, pp. 3017–3025, Jun. 2013.
[96] J. Zhong, A. Johnson, E. A. Alwan, and J. L. Volakis, "Dual-linear polarized phased array with 9:1 bandwidth and 60° scanning off broadside," *IEEE Trans. Antennas Propag.*, vol. 67, no. 3, pp. 1996–2001, Mar. 2019.
[97] A. D. Johnson, J. A. Caripidis, S. B. Venkatakrishnan, M. Ali, and J. L. Volakis, "Deployable inverted-hat monopole with 3:1 constant gain bandwidth," *IEEE Antennas Wireless Propag. Lett.*, vol. 19, no. 6, pp. 935–938, Jun. 2020.
[98] U. D. Silva, S. Pulipati, S. B. Venkatakrishnan, S. Bhardwaj, and A. Madanayake, "A passive STAR microwave circuit for 1-3 GHz self-interference cancellation," in *Proc. IEEE 63rd Int. Midwest Symp. Circuits Syst. (MWSCAS)*, 2020, pp. 105–108.
[99] X.-L. Liang, S.-S. Zhong, and W. Wang, "UWB printed circular monopole antenna," *Microw. Opt. Technol. Lett.*, vol. 48, no. 8, pp. 1532–1534, 2006.
[100] J. Liang, C. Chiau, X. Chen, and C. Parini, "Study of a printed circular disc monopole antenna for UWB systems," *IEEE Trans. Antennas Propag.*, vol. 53, no. 11, pp. 3500–3504, Nov. 2005.
[101] S. S. Bhatia and J. S. Sivia, "A novel design of circular monopole antenna for wireless applications," *Wireless Pers. Commun.*, vol. 91, pp. 1153–1161, Jul. 2016.
[102] N. Akram et al., "Frequency-multiplexed array digitization for MIMO receivers: 4-antennas/ADC at 28 GHz on Xilinx ZCU-1285 RF SoC," *IEEE Access*, vol. 9, pp. 142743–142753, 2021.
[103] N. Akram et al., "Massive-MIMO and digital mm-Wave arrays on RF-SoCs using FDM for M-fold increase in antennas per ADC/DAC," in *Proc. IEEE Space Hardw. Radio Conf. (SHaRC)*, 2021, pp. 25–27.
[104] A. Peram, A. S. Rami Reddy, and M. G. Prasad, "Miniaturized single layer ultra wide band (UWB) patch antenna using a partial ground plane," *Wireless Pers. Commun.*, vol. 106, no. 3, pp. 1275–1291, 2019.
[105] S. Baudha and D. K. Vishwakarma, "Bandwidth enhancement of a planar monopole microstrip patch antenna," *Int. J. Microw. Wireless Technol.*, vol. 8, no. 2, pp. 237–242, 2016.
[106] M. Karimipour and N. Komjani, "Holographic-inspired multibeam reflectarray with linear polarization," *IEEE Trans. Antennas Propag.*, vol. 66, no. 6, pp. 2870–2882, Jun. 2018.
[107] M. Salehi and H. Oraizi, "Holographic transmitarray antenna with linear polarization in X band," *AEU-Int. J. Electron. Commun.*, vol. 146, Mar. 2022, Art. no. 154115.
[108] M. Karimipour and N. Komjani, "Realization of multiple concurrent beams with independent circular polarizations by holographic reflectarray," *IEEE Trans. Antennas Propag.*, vol. 66, no. 9, pp. 4627–4640, Sep. 2018.
[109] Y. Hu, M. Yin, W. Xia, S. Rangan, and M. Mezzavilla, "Multi-frequency channel modeling for millimeter wave and THz wireless communication via generative adversarial networks," 2022, *arXiv:2212.11858*.

SEONGJOON KANG (Graduate Student Member, IEEE) received the B.S. and M.S. degrees in electrical and computer engineering from Seoul National University in 2017 and 2019, respectively. He is currently pursuing the Ph.D. degree with the Tandon School of Engineering, New York University, under the supervision of Prof. S. Rangan. His research interests include UAV and satellite communication, MIMO, and upper mid-band and millimeter wave spectrum management.

MARCO MEZZAVILLA (Senior Member, IEEE) received the B.Sc., M.Sc., and Ph.D. degrees in electrical engineering from the University of Padua, Italy. He held visiting research positions with NEC Network Laboratories, Heidelberg; Centre Tecnològic Telecomunicacions Catalunya, Barcelona, and Qualcomm Research, San Diego. He joined New York University in 2014, where he is currently a Research Faculty. He leads several research projects that focus on upper mid-band, mmWave, and sub-THz radio access technologies for next generation wireless systems. His research interests include communication protocols, wireless prototyping, cybersecurity, and robotics.

SUNDEEP RANGAN (Fellow, IEEE) received the B.A.Sc. degree in electrical engineering from the University of Waterloo, Canada, and the M.Sc. and Ph.D. degrees in electrical engineering from the University of California at Berkeley, Berkeley. He has held postdoctoral appointments with the University of Michigan, Ann Arbor, and Bell Labs. In 2000, he co-founded (with four others) Flarion Technologies, a spin-off of Bell Labs, that developed Flash OFDM, the first cellular OFDM data system and pre-cursor to 4G cellular systems including LTE and WiMAX. In 2006, Flarion was acquired by Qualcomm Technologies. He was a Senior Director of Engineering with Qualcomm involved in OFDM infrastructure products. He joined NYU Tandon (formerly NYU Polytechnic) in 2010, where he is currently a Professor of Electrical and Computer Engineering. He is the Associate Director of NYU WIRELESS, an industry-academic research center on next-generation wireless systems.

ARJUNA MADANAYAKE (Member, IEEE) received the B.Sc. degree in electronic and telecommunication engineering from the University of Moratuwa, Sri Lanka, and the M.Sc. and Ph.D. degrees in electrical engineering from the University of Calgary, Canada. He is an Associate Professor of Electrical and Computer Engineering with Florida International University, Miami, FL. He is the Founder of Arcane AI and Wireless which is a startup focused on commercialization activities for research conducted with RAND Lab. He directs the RF, Analog and Digital Lab, where he advises about 13 Ph.D. students on various topics supported by NSF SWIFT, NSF FuSE, NSF MRI, ONR, NIH, Digital Locations, NTIA, Lockheed Martin, CIA Labs, NSF ICORPS, NSF IUCRC, and NSF SpectrumX. His research areas span the intersection of RF and analog CMOS circuits, digital ASIC and RF-SoC/FPGAs, mixed-signal, and microwave/mm-wave system design. He is interested in arrays, signal processing, and computer architecture. He is a Founding Member of the IEEE Circuits and Systems Education and Outreach Technical Committee, and a member of the IEEE Technical Committee on Digital Signal Processing.

SATHEESH BOJJA VENKATAKRISHNAN (Senior Member, IEEE) was born in Tiruchirappalli, India, in 1987. He received the bachelor's degree in electronics and communication engineering from the National Institute of Technology, Tiruchirappalli, India, in 2009, and the M.S. and Ph.D. degrees in electrical engineering from The Ohio State University, Columbus, OH, USA, in 2017. He was a Scientist with DRDO, India, from 2009 to 2013, working on the development and implementation of active electronic steerable antennas. He is currently an Assistant Professor of Electrical and Computer Engineering with Florida International University, Miami, FL, USA. His current research interests include RF system design for secure wideband communications, data sensing and imaging, interference mitigation techniques, and RFSoC-based simultaneous transmit and receive system to improve the spectral efficiency. In parallel, he has been working on developing RF sensors and circuits, including fully passive neural implants and multimodal patch sensors for bio-medical applications. He was the recipient of numerous awards and recognitions including the IEEE Electromagnetic Theory Symposium 2019 Young Scientist Award, and the Best Paper Award in the International Union of Radio Science General Assembly and Scientific Symposium (USNC–URSI) held in Montreal, Canada, in August 2017. He is a member of Phi Kappa Phi and also an Associate Member of USNC–URSI.

GRÉGORY HELLBOURG received the engineering and M.Sc. degrees in signal and image processing and the Ph.D. degree in signal processing and automation from the University of Orléans, France, in 2010 and 2014, respectively. He is a Staff Scientist with the Cahill Center for Astronomy and Astrophysics, California Institute of Technology, CA, USA, and a Spectrum Manager of the Owens Valley Radio Observatory, CA, USA. He will oversee the main decisions and act as a Project Manager. His expertise lies in signal processing, radio interference detection and mitigation, and system design for radio astronomy.

MONISHA GHOSH (Fellow, IEEE) received the B.Tech. degree from IIT Kharagpur in 1986, and the Ph.D. degree from USC in 1991. She is a Professor of Electrical Engineering with the University of Notre Dame and a member of the Notre Dame Wireless Institute. She is also the Policy Outreach Director for SpectrumX, the first NSF Center for Spectrum Innovation. Prior to joining the University of Notre Dame in 2022, she was the Chief Technology Officer with Federal Communications Commission, a Program Director of the National Science Foundation, a Research Professor with the University of Chicago. She also spent 24 years in industry research at Bell Labs, Philips Research and Interdigital working on a wide variety of wireless systems: HDTV, Wi-Fi, TV white spaces, and cellular. Her research interests are in the development of next generation wireless systems: cellular, Wi-Fi, and loT, with an emphasis on spectrum sharing, coexistence, and applications of machine learning to improve network performance.

HAMED RAHMANI (Member, IEEE) received the B.Sc. degree in electrical and computer engineering from the Sharif University of Technology, Tehran, Iran, the M.Sc. degree in electrical and computer engineering from Rice University, Houston, TX, USA, and the Ph.D. degree in electrical and computer engineering from the University of California Los Angeles. He is an Assistant Professor of Electrical and Computer Engineering with New York University (NYU). Before joining NYU, he held multiple industry and research positions. As a research scientist, he worked with IBM T. J. Research Center in Yorktown Heights, on high-speed electrical/optical interconnects. He was an Adjunct Professor with Columbia University, New York, NY, USA and a Visiting Lecturer with Princeton University, where he offered graduate-level courses in analog and RF circuit design. He was also a Senior RFIC Design Engineer with Qualcomm Inc., where he focused on advanced 5G transmitters for cellular applications and RF front-end designs. He is the recipient of several prestigious awards and fellowships, including the IEEE MTT-S Graduate Fellowship for medical applications and the Texas Instruments Distinguished Fellowship.

ADITYA DHANANJAY received the Ph.D. degree from the Courant Institute of Mathematical Sciences, New York University (NYU), New York, NY, USA. He was involved in mesh radio routing and resource allocation protocols, data communication over cellular voice channels, low-cost wireless rural connectivity, OFDM equalization, and phase noise mitigation in mm-wave networks. He currently holds a postdoctoral position with NYU. He has developed and supervised much of the mm-wave experimental work at the center. He has authored several refereed articles (including at SIGCOMM and MobiCom). He holds one patent and two provisional patents in the millimeter-wave space.